Mechanics Research Communications 127 (2023) 103960

Contents lists available at ScienceDirect

Mechanics Research Communications

journal homepage: www.elsevier.com/locate/mechrescom

# A variational multiscale method for natural convection of nanofluids

Lixing Zhu [a,1], Shoaib A. Goraya [b,2], Arif Masud [b,*]

[a] Institute of Mechanics, Chinese Academy of Sciences, Beijing 100049, China
[b] Department of Civil and Environmental Engineering, University of Illinois at Urbana-Champaign, Urbana, IL 61801-2352, USA

ARTICLE INFO

*Keywords:*
Stabilized methods
Nanofluids
Heat transfer
Boussinesq approximation
Natural convection
Wavy wall
Variational multiscale
Finite elements

ABSTRACT

The notion of enhanced thermal convection via particle laden fluids has been around for a long time. Technological challenges associated with the development of micro to nano particles with desired properties and their uniform dispersion in the base fluid have been a bottleneck. Relatively recently, the advent of modern manufacturing techniques from micro to nanoscales have rekindled interest in this class of fluids for innovative applications in advanced engineering systems.

Buoyancy-induced convection and heat transfer involves conservation laws of mass, momentum, and energy. The mathematical model is comprised of two-way coupled system of mixed-field and convection-dominated partial differential equations. A stabilized method for nonlinearly coupled system is presented, and a systematic approach to develop the sub-grid scale (SGS) physics-based models is described. Explicit structure of the stabilization tensor is derived and it is shown to preserve nonlinear coupling in the SGS models that plays a critical role when nonlinear coupling of mechanical and thermal fields leads to anisotropy across the scales. The formulation is variationally consistent and results in optimal spatial convergence rates on structured meshes for linear triangles and bilinear quadrilaterals. Consistent linearization of the nonlinear system of equations yields quadratic rate of convergence of nonlinear iterations in the Newton-Raphson method. The method is tested on problems with increasing level of complexity to highlight the mathematical attributes of the method and its range of applicability.

## 1. Technical background and perspective

Over a century ago, Maxwell [1] proposed the idea of suspending microscale particles in a base fluid to enhance its heat transfer properties. However, technological limitations of the time precluded reaching the scale of nanosized particles. Microparticles that were used in earlier studies settled rapidly in the fluid causing abrasion and clogging in the flow channels that hindered further research. Nanofluids is a term that was proposed by Choi and Eastman [2] to describe a new kind of heat transfer fluids that contain small quantities of metallic or non-metallic nanoparticles that are scattered homogeneously to produce a continuous phase. Several research studies have highlighted the enhanced thermal conductivity of nanofluids in engineering applications. These include energy storage devices such as the solar thermal collectors, heat transfer devices and heat exchangers, thermal management devices and microchannel heat exchangers in electronic devices [3], automobile radiators, as well as in their innovative use in the air conditioning and refrigeration systems [4]. More recently, hybrid nanofluids that are comprised of two or more nanoparticles mixed in the base fluid, thereby producing a new class of heat transfer fluids that have suspending metallic [5] or oxide [6] nanoparticles as suspension, have shown promising results for applications in the cooling systems [7]. Numerical studies have also been performed on the use of these fluids in a variety of regular and irregular geometries, thus expanding the scope for the application of nanofluids. However, non-conventional shapes like those in biological systems, i.e., blood vessels, and geometries with elastic walls and complex curved boundaries have not been investigated broadly [8].

### 1.1. Preparation of nanofluids

Despite considerable advances in the manufacturing technologies for nanofluids, there are still some limitations. First, nanofluids can become unstable due to the strong Van der Waals interactions and cohesive

* Corresponding author.
*E-mail address:* amasud@illinois.edu (A. Masud).
[1] Former Graduate Research Assistant.
[2] Graduate Research Assistant.

https://doi.org/10.1016/j.mechrescom.2022.103960
Received 22 November 2021; Received in revised form 8 August 2022; Accepted 10 August 2022
Available online 29 September 2022
0093-6413/© 2022 Elsevier Ltd. All rights reserved.

forces between nanoparticles, thereby highlighting the importance of the preparation techniques in producing stable nanofluids. In general, there are two methods for the preparation of nanofluids. The two-step approach which is more common and economical involves preparation of nanoparticles as dry powder before dispersing them into the base fluid by agitation, stirring or ultra-sonication [9]. However, a drawback of this technique is that it often has low stability and a high tendency of particle aggregation. To counter these issues, one-step technique has been proposed in which nanofluids are prepared by direct deposition of the nanoparticles using the physical vapor deposition and liquid chemical methods [10,11]. This method results in more stable nanofluid suspensions than the former method [12]. However, it is not yet scalable and still has stability issues due to aggregation that can be improved by techniques such as adding surfactants, pH modulation, and ultrasonic vibrations [13].

### 1.2. Effects of nanoparticles on thermophysical properties of a nanofluid

Adding nanoparticles to a fluid enhances heat transfer by altering its thermophysical properties that include thermal conductivity, viscosity, density, and specific heat. Many experimental and numerical studies have been carried out to develop correlations of enhancement in thermal conductivity due to the addition of a variety of nanoparticles. Oxide nanoparticles are the most popular and thermal conductivity of the base fluids can be enhanced by 15–40% with their addition [14]. Moreover, nanoparticle shape, size, aggregation, and interfacial thermal resistance also effect the thermal conductivity of a nanofluid [15]. For instance, it has been shown that 1-D network of connected structure of nanoparticle is more effective than the spherical shaped particles [16].

Viscosity has a direct relation with the nanoparticle concentration, while an inverse relation with the temperature of the Newtonian nanofluid. Research studies have shown that for a ZnO-Ag/Water hybrid nanofluid, viscosity enhancement of 80% can be achieved with 2% volume fraction of nanoparticles. Nanofluids with non-aqueous base fluids show non-Newtonian behavior as their viscosity changes with shear rate. Paraffin based nanofluids have shown to have achieved a higher value of viscosity at low shear rates [17]. However, relation between nanoparticle concentration and rheology of the nanofluid is not clear, especially for hybrid nanofluids [4].

Density of a nanofluid generally increases with an increase in volume of nanoparticles. Several correlations have been proposed in the literature in which density also depends on temperature in addition to the nanoparticle volume fraction [18,19]. However, temperature independent relation proposed in [20] is the most widely used in numerical simulations because of its simplicity and acceptable accuracy [12].

In most cases, addition of nanoparticles leads to a reduction in the specific heat. However, this behavior depends on the type of base fluid. A number of relations have been proposed in the literature for the specific heat of different nanofluids that depends on volume concentration of nanofluid, temperature, and size of the nanoparticles [21,22]. The simple weighted average relationship proposed in [22] has been widely used in simulations as it gives good agreement with the experimental data [23].

### 1.3. Models for heat transfer mechanism in nanofluids

There are three categories of heat transfer mechanisms in nanofluids: (i) natural convection, (ii) mixed convection, and (iii) forced convection [24]. The advantages of natural convection compared to forced convection are lower noise, reduced power consumption, and lower required maintenance of the systems that utilize natural convection strategy. Moreover, natural convection occurs due to density variation in the fluid and does not need any external source like a pump or a fan. In this paper, we will focus on the natural convection mechanism in this class of fluids.

Classical theories [25,26,1] have helped explain the thermal conductivity enhancement in fluids with suspensions in the context of Brownian motion. They have also shown to be valid for a wide range of nanoparticle concentrations [25]. Later studies found that Brownian motion alone is not enough to explain the phenomenon [27]. Instead, mechanisms such as liquid layering (nanolayers), thermophoresis, van Der Waals forces, particle nanoclusters, and electro-kinetic effects also contribute to the enhanced thermal conductivity in nanofluids [28–31]. Various models that depend on extension of classical theory, liquid layering, particle aggregation, and particle movement mechanisms have been developed to explain the thermal behavior of nanofluids [28, 32–35]. These models either employ the continuum approach that assumes well-dispersed nanoparticles [36] or the effective medium approach that accounts for local distribution of nanoparticles and therefore predicts enhanced thermal conductivity which is attributed to nanoparticle aggregation [37]. However, for decane-based nanofluids, an experimental study [38] showed no aggregation or sedimentation, thus challenging the previous explanations. Models that are based on Brownian dynamics [37] have also been proposed that have shown good agreement with the experimental data. The success of all these models has been somewhat limited, and no clear picture seems to have emerged until recently [36].

### 1.4. Numerical modelling approaches

There are two main approaches for numerical modeling of nanofluids, namely, single-phase and two-phase modeling methods. In single phase modeling, nanoparticles are assumed to be uniformly dispersed and the slip between the base fluid and the nanoparticles is ignored. The general form of the governing equations is similar to that of conventional fluids, whereas the thermophysical properties of nanofluids are estimated based on the models discussed in the previous sections. There are further three categories of single phase modeling: (i) homogenous, (ii) thermal disruption, and (iii) Boungiorno's model. In the homogenous modeling, the mixture of solid nanoparticles and the base fluid is considered as a single-phase continuum with certain effective material properties that may or may not be temperature dependent. Moreover, the solid and fluid phases are assumed to be in a hydrodynamic and thermal equilibrium. This approach has been most widely used in the literature and is also employed in the model and the numerical method presented in this paper. Use of temperature-dependent relations for thermophysical properties in homogenous models has shown to increase their accuracy. Thermal disruption model is obtained by modifying homogenous single-phase model to account for random and chaotic motion of nanoparticles that enhances heat transfer and induces velocity and temperature perturbations [22]. By considering Brownian and thermophoresis effects, Buongiorno developed a two-component four--equation nonhomogeneous equilibrium model for transport equations in nanofluids [39]. In Buongiorno's model, the effect of the base fluid and the nanoparticle relative velocity is described more mechanistically than in the thermal dispersion model.

In the two-phase approaches, base liquid and nanoparticles are modeled as two separate phases with different velocities and temperatures, such that there is a relative velocity between the particles and the base fluid. The two-phase approaches are categorized in two general groups, known as Eulerian–Eulerian and Eulerian–Lagrangian models. In the Eulerian–Eulerian approach, both the base fluid and the nanoparticles phases are considered as interacting continua. On the other hand, in the Eulerian–Lagrangian approach, the base fluid is a continuum while the nanoparticles are considered as a discrete phase [29].

Since nanofluids are inherently two-phase fluids, two-phase models have more physics embedded in them as compared to the single-phase homogeneous models. They generally perform better when compared with the experimental data, however they are computationally more expensive. On the other hand some numerical studies have also shown that the results of homogeneous models are in fact closer to the experimental data as compared to the two-phase models because of the

uncertainties in mathematical modeling of mechanisms such as sedimentation and aggregation of nanoparticles in the two-phase models [29].

### 1.5. Numerical simulation methods for nanofluids

Several numerical methods have been proposed to simulate flow of nanofluids across a range of material and geometric scales. At macroscale level, finite difference, finite volume, and finite element methods have been used with considerable success. Finite difference method is the simplest of all the methods but it is effective only for the structured meshes [40]. Finite volume method has been widely used in numerical simulations due to its simplicity, less computational cost, and the availability of commercial software packages [41]. However, modeling complex geometries with the finite volume method is considered a difficult task [30]. Finite Element (FE) method is particularly useful for efficient modeling of complicated geometries, and consequently several commercial packages have been developed [30]. A literature review reveals that FE based methods are relatively computationally expensive [30]. In addition, the use of staggered schemes along with a lack of rigorous numerical coupling to solve thermo-mechanically coupled non-linear system of partial differential equations are considered potential bottlenecks for the method. More recently, control volume finite element technique has been proposed that combines the benefits of both the finite volume and finite element methods and has shown to be effective for complex geometries [42].

At mesoscale level, lattice Boltzmann method is usually employed that incorporates microscopic physical interactions of the fluid particles to predict mesoscale thermal behavior and hydrodynamic characteristics [43]. In addition, dissipative particle dynamics is also employed at the mesoscale [44], which is a coarser version of molecular dynamics method and uses randomly distributed particles in the flow domain that preserve conservation of mass, momentum, and energy. Molecular Dynamics Simulations (MDS) are used at microscale in which flow dynamics and interactions of molecules and atoms are computed over a time period using Newton's equations of motion together with molecular mechanics. These approaches are of particular interest at the nanoscale level where the continuum hypothesis of bulk flow region greater than the mean free molecular path no longer remains valid (e.g., flow around carbon nanotubes) [45,46].

## 2. Introduction to stabilized methods for nanofluidics

The challenges in the modeling of nanofluids include bridging the gap between the scales of the modeled physics [29], and accounting for the microscale interaction between nanoparticles and the base fluid [47] in the macroscale fluid dynamics. The modeling strategies for nanofluids can be categorized into two classes: the single-phase approach and the two-phase approach [48]. The single-phase approach treats the dispersed nanoparticles and the base fluid as a mixture with uniformly distributed properties, while the two-phase approach treats the nanoparticles as an independently evolving phase. Since nanoparticles can be comprised of different material types, namely, oxides, metallic particles, another attribute of nanofluids is that they can be stimulated by different external activation mechanisms. The class of ferrofluids that can be activated via magnetic flux draw special attention in many applications, such as biomagnetic [49] and microelectronic systems [50].

The mathematical model of thermal fluids consists of conservation of mass, momentum, and energy [51]. Mass conservation is invariably written as the incompressibility condition, while a Boussinesq buoyancy force is introduced in the momentum balance equation to account for the local variation of temperature. The energy conservation takes the form of convection-diffusion of temperature field where the velocity field is furnished by the Navier-Stokes equations. The mathematical model is a two-way coupled system of mixed-field and convection-dominated equations. Consequently, one needs to address three numerical issues to construct a robust computational framework: (i) the *inf-sup* constraint arising from the mixed field formulation, (ii) the convection-dominant flow in both the equations of momentum and energy balance, and (iii) the coupling strategy between the divergence-free velocity and the temperature fields.

The *inf-sup* constraint has been adequately addressed in the literature. In the context of finite element method, convectional Taylor-Hood and Crouzeix-Raviart elements that satisfy the *inf-sup* constraint are used in the computation of natural convection [40], while the control volume strategy has also been used in similar problems [42]. In the context of finite-volume method, Semi-Implicit Pressure Linked Equations (SIMPLE) algorithm is employed with staggered grids to resolve the numerical difficulties [52,53]. Rhie-Chow interpolation and its derivatives have also been used in the finite-volume method to avoid staggered grids [54,55]. Though these methods are capable of resolving the coupled nonlinear system, they often lack consistency, leading to low computational efficiency in the solution process. The lack of rigorous coupling between numerically computed fields reduces the robustness of the method when applied to higher Reynolds number and Rayleigh number flows.

This paper presents a robust computational method based on Variational Multiscale (VMS) framework [56] to address the numerical issues enumerated above in a unified way. VMS based stabilized methods are well established for convection dominated flow problems [57–59], as well as for mixed-field problems in both fluid mechanics [60,61] and solid mechanics [62,63]. Recently, VMS-based stabilized formulations have been extended to coupled systems where an active scalar field that is governed by a convection-diffusion equation is embedded in the equations for the balance of momentum (i.e., free-surface flows [64,65], and stratified flows [66,67]). The paradigm of VMS framework is based on the variational decomposition of scales, which leads to a systematic approach to recover the sub-grid scale (SGS) physics and project it back on to the resolved scales. Amongst the two approaches to develop the SGS models are: Green's functions based methods [66–68], and residual-free bubbles (RFB) method and its generalizations [58–65]. The later approach preserves the differential operators in the SGS formulation, which leads to stabilization tensors that evolve spatially and temporally as the flow physics evolves. This feature of the formulation is critical for the simulation of thermal fluids where nonlinear coupling of the fields in the system leads to anisotropy across the scales.

An outline of the rest of the paper is as follows: Section 3 describes the governing equations for an incompressible thermal fluid. Section 4 presents derivation of the fully coupled stabilized form. In Section 5, the proposed method is studied numerically via four test cases with increasing degree of complexity in the flow physics. Concluding remarks are presented in Section 6.

## 3. Incompressible thermal fluid with Boussinesq buoyancy

### 3.1. Strong form

In the mathematical model for thermal fluids, energy conservation is introduced in the form of convection-diffusion equation for the temperature field. The spatiotemporally varying temperature field is an active scalar field as it also appears in the conservation of momentum equation. In this paper we focus on steady-state heat transfer wherein convection speed is far less than the acoustic speed with a limited gap between the intensities of thermal sources and sinks. Under these conditions the well-known Boussinesq approximation [51], where a buoyancy force is introduced to represent the thermal effect in the momentum balance equation, suffices to model the physics of the thermal fluids. The governing system of equations for steady-state stratified flows in an open bounded domain $\Omega \in R^{n_{sd}}$ can be written as follows.

$$\mathbf{u}\cdot\nabla\mathbf{u} = -\nabla p + \nabla\cdot(2\nu\nabla^{s}\mathbf{u}) - \mathbf{g}\beta\theta + \mathbf{f}_{b} \tag{1}$$

$$\nabla\cdot\mathbf{u} = 0 \tag{2}$$

$$\mathbf{u}\cdot\nabla\theta - \nabla\cdot(\alpha\nabla\theta) = f \tag{3}$$

where the unknown fields are velocity $\mathbf{u}$, pressure $p$, and the relative temperature $\theta$. $\nu$ is the kinematic viscosity and $\alpha$ is the thermal diffusivity coefficient. The governing system of Eqs. (1)–(3) are the conservation of momentum, mass and energy, respectively. Specifically, a Boussinesq buoyancy term that depends on the gravitational acceleration vector $\mathbf{g}$, the thermal expansion coefficient $\beta$, and the unknown relative temperature field $\theta$ is added to the momentum balance equation. The conservation of mass takes the form of divergence-free constraint in the limit of zero Mach number. In the equation of conservation of energy, the relative temperature field is transported by the velocity field $\mathbf{u}$ furnished by the momentum balance equation. The relative temperature field $\theta = T - T_0$ is defined as the variance of absolute temperature $T$ and the reference temperature $T_0$. The non-gravitational body force $\mathbf{f}_b$ can also incorporate external forcing mechanisms (e.g., Lorentz force), and $f$ is the local heat source/sink. $\nabla^s = (\nabla + \nabla^T)/2$ is the symmetric gradient operator.

The boundary conditions on the domain boundary $\Gamma = \partial\Omega$ are:

$$\mathbf{u}(\mathbf{x}) = \mathbf{g}_M \qquad \text{on } \Gamma_g^M \tag{4}$$

$$\theta(\mathbf{x}) = \mathrm{g_E} \qquad \text{on } \Gamma_{\mathrm{g}}^{\mathrm{E}} \tag{5}$$

$$\boldsymbol{\sigma}\cdot\mathbf{n} = (2\nu\nabla^{\mathrm{s}}\mathbf{u} - \mathrm{p}\mathbf{I})\cdot\mathbf{n} = \mathbf{h}_{\mathrm{M}} \qquad \text{on } \Gamma_{\mathrm{h}}^{\mathrm{M}} \tag{6}$$

$$\boldsymbol{\phi}\cdot\mathbf{n} = \alpha\nabla\theta\cdot\mathbf{n} = h_E \qquad \text{on } \Gamma_h^E \tag{7}$$

where $\mathbf{g}_M$ and $g_E$ are the Dirichlet boundary conditions for velocity field and relative temperature field, while $\mathbf{h}_M$ and $h_E$ are the Neumann boundary conditions for the total stress $\boldsymbol{\sigma}$ and heat flux $\boldsymbol{\phi}$, respectively. $\mathbf{n}$ is the unit outward normal vector at the boundary. Moreover, these boundaries satisfy the following conditions: $\Gamma_g^M \cap \Gamma_h^M = \varnothing$, $\Gamma_g^M \cup \Gamma_h^M = \Gamma$, $\Gamma_g^E \cap \Gamma_h^E = \varnothing$, and $\Gamma_g^E \cup \Gamma_h^E = \Gamma$.

In this paper, we employ the single-phase approach to model natural convection of nanofluids. The single-phase approach utilizes the homogenized material properties of the base fluid and solid particles to represent the fluid parameters of the resulting nanofluid. The material properties of the mixture depend on the volume fraction of nanoparticles only. As mentioned in the introduction, this type of modeling strategy is based on the following assumptions: (i) nanoparticles have uniform geometric attributes, (ii) nanoparticles are uniformly dispersed, and (iii) the base fluid and nanoparticles have reached thermal equilibrium state.

We now present the homogenization of the nanofluid properties. The density $\rho$ and heat capacity $\rho C_p$ are modeled via weighted averaging.

$$\begin{aligned} \rho_{nf} &= (1-\phi)\rho_{bf} + \phi\rho_{np} \\ (\rho C_p)_{nf} &= (1-\phi)(\rho C_p)_{bf} + \phi(\rho C_p)_{np} \end{aligned} \tag{8}$$

We adopt Brinkman's model [69] to calculate the dynamic viscosity of the mixture, which is suitable for small rigid spherical particles.

$$\mu_{nf} = \frac{\mu_{bf}}{(1-\phi)^{5/2}} \tag{9}$$

The thermal conductivity of the nanofluid defined in [46] is as follows.

$$\frac{k_{nf}}{k_{bf}} = \frac{(k_{np}+2k_{bf}) - 2\phi(k_{bf}-k_{np})}{(k_{np}+2k_{bf}) + \phi(k_{bf}-k_{np})} \tag{10}$$

Accordingly, the kinematic viscosity and the thermal diffusivity are calculated as follows.

$$\begin{aligned} \nu_{nf} &= \frac{\mu_{nf}}{\rho_{nf}} \\ \alpha_{nf} &= \frac{k_{nf}}{(\rho C_p)_{nf}} \end{aligned} \tag{11}$$

The subscripts $(\cdot)_{nf}$, $(\cdot)_{bf}$, and $(\cdot)_{np}$ in Eqs. (8)–(11) denote the corresponding material parameter of the nanofluid, the base fluid and the nanoparticles, respectively. The thermal expansion $\beta_{nf}$ is scaled in two different ways in the literature:

$$\beta_{nf} = \beta_{bf}(1-\phi) + \beta_{np}\phi \tag{12}$$

$$\beta_{nf} = \frac{(1-\phi)(\rho\beta)_{bf} + \phi(\rho\beta)_{np}}{\rho_{nf}} \tag{13}$$

where Eq. (12) is used in [70,71] and Eq. (13) is used in [42].

### 3.2. Standard weak form

The functional spaces $\mathscr{U}, \mathscr{P}, \mathscr{T}$ appropriate for the velocity, pressure and temperature trial solutions are defined as follows:

$$\mathscr{U} = \left\{\mathbf{u} | \mathbf{u} \in \left(H^1(\Omega)\right)^{n_{sd}}, \mathbf{u} = \mathbf{g}_{\mathbf{M}} \text{ on } \Gamma_{\mathbf{g}}^{\mathbf{M}}\right\} \tag{14}$$

$$\mathscr{P} = \{p | p \in (L_2(\Omega))^{n_{sd}}\} \tag{15}$$

$$\mathscr{T} = \left\{\theta | \theta \in \left(H^1(\Omega)\right)^{n_{sd}}, \theta = \mathrm{g}_E \text{ on } \Gamma_g^E\right\} \tag{16}$$

where $L_2(\Omega)$ and $H^1(\Omega)$ are the standard Sobolev spaces. Let $\mathbf{w}(\mathbf{x}) \in \mathscr{W} = (H_0^1(\Omega))^{n_{sd}}$, $q(\mathbf{x}) \in \mathscr{Q} = C^0(\Omega) \cap L^2(\Omega)$, and $\eta(\mathbf{x}) \in \mathscr{H} = H_0^1(\Omega)$ be the weighting functions for the velocity $\mathbf{u}$, kinematic pressure $p$, and relative temperature $\theta$, respectively. The spaces of weighting functions $\mathscr{W}, \mathscr{Q}, \mathscr{H}$ satisfy the homogenous part of the essential boundary conditions.

The standard weak form of the problem is: Find $\mathbf{V} = (\mathbf{u}, p, \theta) \in \mathscr{U} \times \mathscr{P} \times \mathscr{T}$, such that $\forall \mathbf{W} = (\mathbf{w}, q, \eta) \in \mathscr{W} \times \mathscr{Q} \times \mathscr{H}$

$$(\mathbf{w}, \mathbf{u}\cdot\nabla\mathbf{u}) + (\nabla\mathbf{w}, 2\nu\nabla^s\mathbf{u}) - (\nabla\cdot\mathbf{w}, p) + (\mathbf{w}, \mathbf{g}\beta\theta) = (\mathbf{w}, \mathbf{h}_M)_{\Gamma_h^M} + (\mathbf{w}, \mathbf{f}_b) \tag{17}$$

$$(q, \nabla\cdot\mathbf{u}) = 0 \tag{18}$$

$$(\eta, \mathbf{u}\cdot\nabla\theta) + (\nabla\eta, \alpha\nabla\theta) = (\eta, h_E)_{\Gamma_h^E} + (\eta, f) \tag{19}$$

## 4. Variational multiscale method

### 4.1. Variational multiscale decomposition

We employ the variational multiscale framework [56,72] to develop the stabilized method and introduce an additive decomposition of the velocity and temperature fields $\{\mathbf{u}, \theta\}$ as well as their corresponding weighting functions $\{\mathbf{w}, \eta\}$:

$$\mathbf{u}(\mathbf{x}) = \bar{\mathbf{u}}(\mathbf{x}) + \mathbf{u}'(\mathbf{x}) \qquad \theta(\mathbf{x}) = \bar{\theta}(\mathbf{x}) + \theta'(\mathbf{x}) \tag{20}$$

$$\mathbf{w}(\mathbf{x}) = \bar{\mathbf{w}}(\mathbf{x}) + \mathbf{w}'(\mathbf{x}) \qquad \boldsymbol{\eta}(\mathbf{x}) = \bar{\boldsymbol{\eta}}(\mathbf{x}) + \boldsymbol{\eta}'(\mathbf{x}) \tag{21}$$

By the additive nature of the decomposition of weighting function in (21), we can split the weak form into coarse-scale and fine-scale problems via grouping the terms based on the weighting functions of either scale:

Coarse-scale coupled problem

$$(\bar{\mathbf{w}}, \mathbf{u}\cdot\nabla\mathbf{u}) + (\nabla\bar{\mathbf{w}}, 2\nu\nabla^s\mathbf{u}) - (\nabla\cdot\bar{\mathbf{w}}, p) + (\bar{\mathbf{w}}, \mathbf{g}\beta\theta) = (\bar{\mathbf{w}}, \mathbf{h}_M)_{\Gamma_h^M} + (\bar{\mathbf{w}}, \mathbf{f}_b) \tag{22}$$

$$(q, \nabla\cdot\mathbf{u}) = 0 \tag{23}$$

$$(\bar{\eta}, \mathbf{u}\cdot\nabla\theta) + (\nabla\bar{\eta}, \alpha\nabla\theta) = (\bar{\eta}, h_E)_{\Gamma_h^E} + (\bar{\eta}, f) \tag{24}$$

Fine-scale coupled problem

$$(\mathbf{w}', \mathbf{u}\cdot\nabla\mathbf{u}) + (\nabla\mathbf{w}', 2\nu\nabla^s\mathbf{u}) - (\nabla\cdot\mathbf{w}', p) + (\mathbf{w}', \mathbf{g}\beta\theta) = (\mathbf{w}', \mathbf{f}_b) \tag{25}$$

$$(\eta', \mathbf{u}\cdot\nabla\theta) + (\nabla\eta', \alpha\nabla\theta) = (\eta', f) \tag{26}$$

where fine-scale fields are assumed to be zero on the domain boundary.

### 4.2. Solution of the fine-scale coupled problem

This section provides a systematic procedure for the derivation of the models for the fine-scale velocity and temperature fields. These models when embedded in the coarse scale weak form not only make the resulting formulation stable in the sense of *inf-sup* stability condition but also address issues that arise in the case of high advection velocity.

To make the fine scale problem tractable we make some simplifying assumptions. The bounded domain $\Omega$ is considered to be the union of non-overlapping subdomains $\Omega'$ with boundary $\Gamma'$, such that $\Omega = \cup_1^n\ \Omega'$ and $n$ is the total number of subdomains. We assume that the fine-scale weighting functions and trial solutions vanish at the subdomain boundaries, namely, $\mathbf{w}' = \mathbf{u}' = \mathbf{0}$ on $\Gamma'$ and $\theta' = \eta' = 0$ on $\Gamma'$.

The fine-scale sub-problem presented in Eqs. (25) and (26) yields a nonlinear coupled system. By resolving the fine-scale problem, we expect to construct the projection from the residual of the coarse-scale Euler-Lagrange equations to the fine-scale solution fields $\mathbf{V}' = \{\mathbf{u}', \theta'\}$. To make the modeling of the projection feasible, we first linearize the fine-scale problem with respect to the fine-scale velocity and relative temperature fields. The fine-scale weak forms in Eqs. (25) and (26) can be written in the following residual form.

$$\begin{aligned} \mathscr{R}'_M(\mathbf{w}'; \bar{\mathbf{u}}, \mathbf{u}', p, \bar{\theta}, \theta') &= (\mathbf{w}', \mathbf{u}\cdot\nabla\mathbf{u}) + (\nabla\mathbf{w}', 2\nu\nabla^s\mathbf{u}) \\ &\quad - (\nabla\cdot\mathbf{w}', p) + (\mathbf{w}', \mathbf{g}\beta\theta) - (\mathbf{w}', \mathbf{f}_b) = 0 \\ \mathscr{R}'_E(\eta'; \bar{\mathbf{u}}, \mathbf{u}', \bar{\theta}, \theta') &= (\eta', \mathbf{u}\cdot\nabla\theta) + (\nabla\eta', \alpha\nabla\theta) - (\eta', f) = 0 \end{aligned} \tag{27}$$

where $\mathscr{R}'_M$ and $\mathscr{R}'_E$ are the residual weak forms of fine-scale conservation of momentum and energy, respectively. It is important to note that the right-hand side terms contain the full fields i.e., coarse and fine fields in the solution slots. The linearization operators are defined as follows.

$$\begin{aligned} \mathscr{L}\left(\mathscr{R}'_M(\mathbf{w}'; \bar{\mathbf{u}}, \mathbf{u}', p, \bar{\theta}, \theta')\right) &= \frac{d}{d\varepsilon}\mathscr{R}'_M(\mathbf{w}'; \bar{\mathbf{u}}, \mathbf{u}' + \varepsilon\delta\mathbf{u}', p, \bar{\theta}, \theta' + \varepsilon\delta\theta')\Big|_{\varepsilon=0} \\ \mathscr{L}\left(\mathscr{R}'_E(\eta'; \bar{\mathbf{u}}, \mathbf{u}', \bar{\theta}, \theta')\right) &= \frac{d}{d\varepsilon}\mathscr{R}'_E(\eta'; \bar{\mathbf{u}}, \mathbf{u}' + \varepsilon\delta\mathbf{u}', \bar{\theta}, \theta' + \varepsilon\delta\theta')\Big|_{\varepsilon=0} \end{aligned} \tag{28}$$

Applying the linearization operators defined in Eq. (28) to the residual weak form in Eq. (27), we obtain the linearized fine-scale weak forms as follows.

$$\begin{aligned} &(\mathbf{w}', \delta\mathbf{u}'\cdot\nabla\bar{\mathbf{u}}) + (\mathbf{w}', \bar{\mathbf{u}}\cdot\nabla\delta\mathbf{u}') + (\nabla\mathbf{w}', 2\nu\nabla^s\delta\mathbf{u}') + (\mathbf{w}', \mathbf{g}\beta\delta\theta') \\ &\quad = -(\mathbf{w}', \bar{\mathbf{u}}\cdot\nabla\bar{\mathbf{u}}) - (\nabla\mathbf{w}', 2\nu\nabla^s\bar{\mathbf{u}}) + (\nabla\cdot\mathbf{w}', p) \\ &\qquad - (\mathbf{w}', \mathbf{g}\beta\bar{\theta}) + (\mathbf{w}', \mathbf{f}_b) \\ &\quad = -(\mathbf{w}', \bar{\mathbf{r}}_M) \end{aligned} \tag{29}$$

$$\begin{aligned} &(\eta', \delta\mathbf{u}'\cdot\nabla\bar{\theta}) + (\eta', \bar{\mathbf{u}}\cdot\nabla\delta\theta') + (\nabla\eta', \alpha\nabla\delta\theta') \\ &\quad = -(\eta', \bar{\mathbf{u}}\cdot\nabla\bar{\theta}) - (\nabla\eta', \alpha\nabla\bar{\theta}) + (\eta', f) \\ &\quad = -(\eta', \bar{r}_E) \end{aligned} \tag{30}$$

where $\bar{\mathbf{r}}_M = \mathbf{r}_M(\bar{\mathbf{u}}, p, \bar{\theta})$ is the residual of the Euler-Lagrange equations of the coarse-scale conservation of momentum, and $\bar{r}_E = r_E(\bar{\mathbf{u}}, \bar{\theta})$ is the residual of the Euler-Lagrange equation of the coarse-scale conservation of energy. These are defined as,

$$\mathbf{r}_M(\bar{\mathbf{u}}, p, \bar{\theta}) = \bar{\mathbf{u}}\cdot\nabla\bar{\mathbf{u}} + \nabla p - \nabla\cdot(2\nu\nabla^s\bar{\mathbf{u}}) + \mathbf{g}\beta\bar{\theta} - \mathbf{f}_b \tag{31}$$

$$r_E(\bar{\mathbf{u}}, \bar{\theta}) = \bar{\mathbf{u}}\cdot\nabla\bar{\theta} - \nabla\cdot(\alpha\nabla\bar{\theta}) - f \tag{32}$$

We follow along the lines of [72] and employ functions $b'(\boldsymbol{\xi})$ that are defined over subdomains $\Omega'$ to interpolate the fine-scale trial solutions and weighting functions as follows.

$$\delta\mathbf{u}' = b'(\boldsymbol{\xi})\mathbf{a}', \quad \mathbf{w}' = b'(\boldsymbol{\xi})\mathbf{c}', \quad \delta\theta' = b'(\boldsymbol{\xi})m', \quad \eta' = b'(\boldsymbol{\xi})n' \tag{33}$$

where the superscript $(\cdot)'$ in Eq. (33) denotes the subdomain-wise quantity. $\mathbf{a}'$ and $m'$ are the coefficients of fine scale fields at the virtual node. By substituting the functions employed for fine-scale fields from Eq. (33) into Eqs. (29) and (30), and applying mean value theorem, the steady-state linearized fine-scale mixed field problem can be written in the form of a linear system as follows:

$$\begin{bmatrix} \widehat{\boldsymbol{\tau}}_M & \widehat{\boldsymbol{\tau}}_{ME} \\ \widehat{\boldsymbol{\tau}}_{EM} & \widehat{\tau}_E \end{bmatrix} \begin{bmatrix} \mathbf{a}' \\ m' \end{bmatrix} = -\begin{bmatrix} (b', \bar{\mathbf{r}}_M) \\ (b', \bar{r}_E) \end{bmatrix} \cong -(-b', 1)\mathbf{I}_{4\text{x}4} \begin{bmatrix} \bar{\mathbf{r}}_M \\ \bar{r}_E \end{bmatrix} \tag{34}$$

where the explicit form of various terms in Eq. (34) are:

$$\widehat{\boldsymbol{\tau}}_{M(n_{sd}\times n_{sd})} = \int_{\Omega^e} \left(\nu\nabla b'\cdot\nabla b'\mathbf{I} + (b')^2\nabla^T\bar{\mathbf{u}} + b'\bar{\mathbf{u}}\cdot\nabla b'\mathbf{I} + \nu\nabla b' \otimes \nabla b'\right)d\Omega \tag{35}$$

$$\widehat{\tau}_{E(1\times 1)} = \int_{\Omega^e} (b'\bar{\mathbf{u}}\cdot\nabla b' + \alpha\nabla b'\cdot\nabla b')d\Omega \tag{36}$$

$$\widehat{\boldsymbol{\tau}}_{ME(n_{sd}\times 1)} = \int_{\Omega^e} \mathbf{g}\beta(b')^2 d\Omega \tag{37}$$

$$\widehat{\boldsymbol{\tau}}_{EM(1\times n_{sd})} = \int_{\Omega^e} (b')^2\nabla^T\bar{\theta}d\Omega \tag{38}$$

where $\widehat{\boldsymbol{\tau}}_M$ is the tensor that relates the fine-scale velocity and the residual of coarse-scale equation of momentum balance. The physical interpretation of $\widehat{\boldsymbol{\tau}}_M$ includes the sweeping effect (i.e., the fine-scale velocity transported by the coarse-scale velocity), the distortion effect (i.e., the coarse-scale velocity transported by the coarse-scale velocity), and the fine-scale diffusion; $\widehat{\tau}_E$ is the parameter that relates the fine-scale temperature and the residual of the coarse-scale equation of the conservation of energy. They are form identical to the fine-scale system of linearized Navier-Stokes equations, and a generic advection-diffusion equation, from our earlier works [58,61,64].

An important contribution in this work is the delineation that in order to derive analytical expressions for the fine-scale models, it is crucial to consider the coupled form of the equations even at the fine-scale variational level. This coupling of the fields results in the cross-coupling terms (i.e., $\widehat{\boldsymbol{\tau}}_{ME}$ and $\widehat{\boldsymbol{\tau}}_{EM}$) of the mechanical phase and thermal phase even in the fine-scale problem. Consequently, full $(n_{sd}+1)\times(n_{sd}+1)$ stability tensor is derived from the linear system in Eq. (34). Hereon, the incremental fine-scale velocities and temperature are written in the residual-driven form as,

$$\begin{bmatrix} \delta\mathbf{u}' \\ \delta\theta' \end{bmatrix}_{n+1} = b^e \begin{bmatrix} \mathbf{a}' \\ m' \end{bmatrix}_{n+1} = \underbrace{-b^e(b^e, 1)\left\{\begin{bmatrix} \widehat{\boldsymbol{\tau}}_M & \widehat{\boldsymbol{\tau}}_{ME} \\ \widehat{\boldsymbol{\tau}}_{EM} & \widehat{\tau}_E \end{bmatrix}\right\}^{-1}}_{\boldsymbol{\tau}} \begin{bmatrix} \bar{\mathbf{r}}_M \\ \bar{r}_E \end{bmatrix}_{n+1} \tag{39}$$

*Remark 1:* The inversion operation in Eq. (39) is achieved through solving the system in Eq. (34). To avoid the zero value in the diagonal terms due to the orthogonality of fine-scale function and its derivatives, we use advection bubble in the weighting slot of the skew advection term, as presented in [58,61,64].

### 4.3. Stabilized coarse-scale formulation

Similarly, we linearize the nonlinear coarse-scale sub-problems in

Eqs. (22)–(24) with respect to the fine-scale velocity and temperature fields. The coarse-scale weak forms are rewritten in the residual form as follows.

$$\begin{aligned}
\mathscr{R}_M(\bar{\mathbf{w}};\bar{\mathbf{u}},\mathbf{u}',p,\bar{\theta},\theta') &= (\bar{\mathbf{w}},\mathbf{u}\cdot\nabla\mathbf{u}) + (\nabla\bar{\mathbf{w}},2\nu\nabla^s\mathbf{u}) \\
&\quad - (\nabla\cdot\bar{\mathbf{w}},p) + (\bar{\mathbf{w}},\mathbf{g}\beta\theta) - (\bar{\mathbf{w}},\mathbf{f}_b) - (\bar{\mathbf{w}},\mathbf{h}_M)_{\Gamma_h^M} \\
\mathscr{R}_C(q;\bar{\mathbf{u}},\mathbf{u}') &= (q,\nabla\cdot\mathbf{u}) \\
\mathscr{R}_E(\bar{\eta};\bar{\mathbf{u}},\mathbf{u}',\bar{\theta},\theta') &= (\bar{\eta},\mathbf{u}\cdot\nabla\theta) + (\nabla\bar{\eta},\alpha\nabla\theta) - (\bar{\eta},f) - (\bar{\eta},h_E)_{\Gamma_h^E}
\end{aligned} \tag{40}$$

where $\mathscr{R}_M$, $\mathscr{R}_C$, and $\mathscr{R}_E$ are the residual weak forms of coarse-scale conservation of momentum, mass, and energy, respectively. Again, the terms on the right-hand side contain both the coarse and fine scale trial solution fields. The linearization operators are defined as follows.

$$\begin{aligned}
\mathscr{L}(\mathscr{R}_M(\bar{\mathbf{w}};\bar{\mathbf{u}},\mathbf{u}',p,\bar{\theta},\theta')) &= \frac{d}{d\varepsilon}\mathscr{R}_M(\bar{\mathbf{w}};\bar{\mathbf{u}},\mathbf{u}'+\varepsilon\delta\mathbf{u}',p,\bar{\theta},\theta'+\varepsilon\delta\theta')\Big|_{\varepsilon=0} \\
\mathscr{L}(\mathscr{R}_C(q;\bar{\mathbf{u}},\mathbf{u}')) &= \frac{d}{d\varepsilon}\mathscr{R}_C(q;\bar{\mathbf{u}},\mathbf{u}'+\varepsilon\delta\mathbf{u}')\Big|_{\varepsilon=0} \\
\mathscr{L}(\mathscr{R}_E(\bar{\eta};\bar{\mathbf{u}},\mathbf{u}',\bar{\theta},\theta')) &= \frac{d}{d\varepsilon}\mathscr{R}_E(\eta;\bar{\mathbf{u}},\mathbf{u}'+\varepsilon\delta\mathbf{u}',\bar{\theta},\theta'+\varepsilon\delta\theta')\Big|_{\varepsilon=0}
\end{aligned} \tag{41}$$

By applying the linearization operators in Eq. (41) to the coarse-scale residual weak form in Eq. (40), we obtain the coarse-scale linearized formulations as follows.

$$\begin{aligned}
&(\bar{\mathbf{w}},\bar{\mathbf{u}}\cdot\nabla\bar{\mathbf{u}}) + (\nabla\bar{\mathbf{w}},2\nu\nabla^s\bar{\mathbf{u}}) - (\nabla\cdot\bar{\mathbf{w}},p) + (\bar{\mathbf{w}},\mathbf{g}\beta\bar{\theta}) + (\bar{\mathbf{w}},\delta\mathbf{u}'\cdot\nabla\bar{\mathbf{u}}) \\
&\quad + (\bar{\mathbf{w}},\bar{\mathbf{u}}\cdot\nabla\delta\mathbf{u}') + (\nabla\bar{\mathbf{w}},2\nu\nabla^s\delta\mathbf{u}') + (\bar{\mathbf{w}},\mathbf{g}\beta\delta\theta') \\
&\quad = (\bar{\mathbf{w}},\mathbf{h}_M)_{\Gamma_h^M} + (\bar{\mathbf{w}},\mathbf{f}_b)
\end{aligned} \tag{42}$$

$$(q,\nabla\cdot\bar{\mathbf{u}}) + (q,\nabla\cdot\delta\mathbf{u}') = 0 \tag{43}$$

$$\begin{aligned}
&(\bar{\eta},\bar{\mathbf{u}}\cdot\nabla\bar{\theta}) + (\nabla\bar{\eta},\alpha\nabla\bar{\theta}) + (\bar{\eta},\delta\mathbf{u}'\cdot\nabla\bar{\theta}) + (\bar{\eta},\bar{\mathbf{u}}\cdot\nabla\delta\theta') + (\nabla\bar{\eta},\alpha\nabla\delta\theta') \\
&\quad = (\bar{\eta},h_E)_{\Gamma_h^E} + (\bar{\eta},f)
\end{aligned} \tag{44}$$

We now combine the resulting formulation of Eqs. (42)–(44) and then group the terms that depend on the fine-scale trial solutions.

$$\begin{aligned}
&(\bar{\mathbf{w}},\bar{\mathbf{u}}\cdot\nabla\bar{\mathbf{u}}) + (\nabla\bar{\mathbf{w}},2\nu\nabla^s\bar{\mathbf{u}}) + (q,\nabla\cdot\bar{\mathbf{u}}) - (\nabla\cdot\bar{\mathbf{w}},p) + (\bar{\eta},\bar{\mathbf{u}}\cdot\nabla\bar{\theta}) + (\nabla\bar{\eta},\alpha\nabla\bar{\theta}) \\
&\quad + (\bar{\mathbf{w}},\mathbf{g}\beta\bar{\theta}) + (\boldsymbol{\chi}_M,\delta\mathbf{u}') + (\chi_E,\delta\theta') \\
&\quad = (\bar{\mathbf{w}},\mathbf{h}_M)_{\Gamma_h^M} + (\bar{\mathbf{w}},\mathbf{f}_b) + (\bar{\eta},h_E)_{\Gamma_h^E} + (\bar{\eta},f)
\end{aligned} \tag{45}$$

where,

$$\boldsymbol{\chi}_M = -\bar{\mathbf{u}}\cdot\nabla\bar{\mathbf{w}} + \bar{\mathbf{w}}\cdot\nabla^T\bar{\mathbf{u}} - \nu(\nabla(\nabla\cdot\bar{\mathbf{w}}) + \Delta\bar{\mathbf{w}}) - \nabla q + \bar{\eta}\nabla^T\bar{\theta}$$

$$\chi_E = \mathbf{g}\beta\bar{\mathbf{w}} - \bar{\mathbf{u}}\cdot\nabla\bar{\eta} - \alpha\Delta\bar{\eta}$$

By substituting the fine-scale solutions defined in Eq. (39) into the corresponding slots in coarse-scale formulation, we arrive at the final stabilized form that is expressed in the residual form as follows. Formal statement is: Find $\mathbf{V} = (\mathbf{u},p,\theta) \in \mathscr{U}\times\mathscr{P}\times\mathscr{T}$, such that $\forall\mathbf{W} = (\mathbf{w},q,\eta) \in \mathscr{W}\times\mathscr{Q}\times\mathscr{H}$, the following holds.

$$\begin{aligned}
&\mathcal{R}^{Gal}(\mathbf{w},q,\eta;\mathbf{u},p,\theta) + \mathcal{R}^{VMS}(\mathbf{w},q,\eta;\mathbf{u},p,\theta) \\
&\quad = \mathcal{F}^{Gal}(\mathbf{w},\eta)
\end{aligned} \tag{46}$$

where,

$$\begin{aligned}
\mathscr{R}^{Gal}(\mathbf{w},q,\eta;\mathbf{u},p,\theta) &= \mathscr{R}_M^{Gal}(\mathbf{w};\mathbf{u},\theta) + \mathscr{R}_C^{Gal}(q;\mathbf{u}) \\
&\quad + \mathscr{R}_E^{Gal}(\eta;\mathbf{u},\theta) \\
\mathscr{R}^{VMS}(\mathbf{w},\eta;\mathbf{u},\theta) &= \left([\boldsymbol{\chi}_M,\chi_E]^T,\boldsymbol{\tau}[\mathbf{r}_M,r_E]\right) \\
\mathscr{R}_M^{Gal}(\mathbf{w};\mathbf{u},\theta) &= (w,\mathbf{u}\cdot\nabla\mathbf{u}) + (\nabla\mathbf{w},2\nu\nabla^s\mathbf{u}) \\
&\quad - (\nabla\cdot\mathbf{w},p) + (\mathbf{w},\mathbf{g}\beta\theta) \\
\mathscr{R}_E^{Gal}(\eta;\mathbf{u},\theta) &= (\eta,\mathbf{u}\cdot\nabla\theta) + (\nabla\eta,\alpha\nabla\theta) \\
\mathscr{R}_C^{Gal}(q;\mathbf{u}) &= (q,\nabla\cdot\mathbf{u}) \\
\mathscr{F}^{Gal}(\mathbf{w},q,\eta) &= (\mathbf{w},\mathbf{h}_M)_{\Gamma_h^M} + (\mathbf{w},\mathbf{f}_b) \\
&\quad + (\eta,h_E)_{\Gamma_h^E} + (\eta,f)
\end{aligned}$$

*Remark 2:* Since the stabilized form Eq. (46) is fully represented in the terms of coarse-scale fields, we drop the superposed bar from the coarse-scale weighting function and trial solutions perturbation notation $\delta$ before fine-scale trial solution fields.

*Remark 3:* For ease of numerical implementation, the subdomain $\Omega'$ in the fine scale problem is taken as the domain of an individual element. Therefore, fine-scale functions take the form of bubble functions that are non-zero over the element and become zero at the element boundary. See e.g. [58,61] for further details.

## 5. Numerical tests

This section presents numerical test cases that establish variational consistency of the method and provide validation of the computed physics. A unique feature of stabilized methods for mixed field problems is that they are free of the constraints imposed by the *inf-sup* stability conditions on the admissible discrete spaces of functions for the various fields. The stabilized formulation developed herein results in a fully coupled method where all the unknown fields are solved concurrently, while using equal-order interpolation functions for the velocity, pressure, and temperature fields.

Variational consistency of the method also results in optimal convergence rates that are attained in the mesh refinement study. Furthermore, consistent linearization of the residual (46) results in quadratic convergence of the solution in the Newton-Raphson loop within each load step (Table 5). We have employed a direct solver (SuperLU) to solve the discretized linear system in each iteration within the Newton-Raphson loop where the tolerance criterion for the relative energy is set equal to $10^{-16}$. The algorithmic form of the solution procedure is presented as Algorithm 1.

There are two dimensionless parameters, namely, Prandtl number ($Pr$) and Rayleigh number ($Ra$) that are used in the test cases presented here. By introducing the characteristic length scale $L_0$, temperature scale $\Delta T$, and velocity scale $U_0$, the two classic non-dimensional numbers are defined as,

$$Pr = \frac{\nu}{\alpha} \quad \text{Prandtl Number} \tag{47}$$

$$Ra = \frac{\beta\Delta T L_0^3|\mathbf{g}|}{\nu\alpha} \quad \text{Rayleigh Number} \tag{48}$$

Algorithm 1

**input:** initial guess $\{\mathbf{u}_0,p_0,\theta_0\}$
Initialize the iteration counter $i \leftarrow 0$
Compute initial residual $R = \|\mathbf{R}_o\|_2$ from Eq. (46)
Newton-Raphson Loop
**while** $\|\mathbf{R}_i\|_2 \geq tol.R_0$ **do**
Compute stabilization tensor $\boldsymbol{\tau}_i$ in Eq. (39) using Eqs. (35)–(38), where $i$ is the iteration counter.
Compute the residual $\mathbf{R}_i$ using Eq. (46).
Compute consistent tangent $K_{pq}^i = -\partial R_p^i/\partial V_q^i$, where $p$, $q$ are indices for the global system and $\mathbf{V}$ is the vector of incremental velocity, pressure, and temperature fields.
Solve linearized system: $\mathbf{K}_i[\Delta\mathbf{u}_i,\Delta p_i,\Delta\theta_i]^T = \mathbf{R}_i$

(*continued on next page*)

(*continued*)

Update solution fields: $\mathbf{u}_{i+1} = \mathbf{u}_i + \Delta\mathbf{u}_i$; $p_{i+1} = p_i + \Delta p_i$; $\theta_{i+1} = \theta_i + \Delta\theta_i$.
Update the iteration counter: $i \leftarrow i + 1$
**end**
**output**: $\{\mathbf{u}, p, \theta\}$

### 5.1. Beltrami flow with analytical solution

We employ a sub-class of the Beltrami flows [40] to investigate the variational consistency of the proposed stabilized formulation via a convergence rate study. The analytical expressions for the velocity, pressure, and relative temperature fields of the flow are as follows,

$$\mathbf{u}^e(x,y) = [-\cos(\pi x)\sin(\pi y),\ \sin(\pi x)\cos(\pi y)]^T \tag{49}$$

$$p^e(x,y) = -\frac{1}{4}(\cos(2\pi x) + \cos(2\pi y)) \tag{50}$$

$$\theta^e(x,y) = \cos(\pi x)\cos(\pi y) \tag{51}$$

and the non-gravitational body forces and heat source driving the flow are as follows,

$$\mathbf{f}_b(x,y) = \begin{bmatrix} -2\pi^2 \nu cos(\pi x)\sin(\pi y) + g_1\beta\cos(\pi x)\cos(\pi y) \\ 2\pi^2 \nu sin(\pi x)\cos(\pi y) + g_2\beta\cos(\pi x)\cos(\pi y) \end{bmatrix} \tag{52}$$

$$f(x,y) = 2\pi^2\alpha\cos(\pi x)\cos(\pi y) \tag{53}$$

The computational domain is a bi-unit square $\Omega = [-1, 1] \times [-1, 1]$ with domain boundaries $\Gamma = \partial\Omega$ that are applied with Dirichlet boundary conditions $\mathbf{g}(\mathbf{x}) = [\mathbf{u}^e, p^e, \theta^e]|_{\boldsymbol{x} \in \Gamma}$ for the velocity, pressure, and relative temperature fields. All the material parameters for this problem are taken as unity. The exact solution and boundary conditions are shown in Fig. 1.

A convergence study is performed using 10×10, 20×20, 30×30, and 40×40 grids employing linear quadrilateral (Q4) and triangular (T3) elements. Figs. 2 and 3 show the convergence rate plots of velocity, pressure, and temperature fields for Q4 and T3 elements, respectively, and optimal rates are obtained for all the test cases which confirms the stability and variational consistency of the formulation.

### 5.2. Rayleigh-Bénard convection: a benchmark case

In this subsection, we investigate the classic Rayleigh-Bénard convection in a 2D bi-unit domain. The schematic diagram and boundary conditions are described in Fig. 4. The problem is driven by applying Dirichlet boundary condition for the relative temperature field at the left and right walls. The top and bottom surfaces are adiabatic walls. All four walls are applied with no-slip boundary condition, and a zero-pressure reference is applied at the left-bottom corner to filter out the constant in the pressure mode. The unit gravity force acts uniformly downwards (negative $y$ direction) and the thermal expansion coefficient $\beta$ is set equal to 1. The Prandtl number is set equal to 0.71 and it corresponds to the physics of the flow of air. Rayleigh number is adjusted by proportionally changing the value of kinematic viscosity $\nu$ and thermal diffusivity $\alpha$.

The exact solution for natural convection has been presented in [39] for $Ra \to 0$, however cases that are of particular interest from an engineering viewpoint are at much higher Rayleigh number for which an analytical solution does not exist. Therefore, for the convergence rate study reported in this subsection, we compare our results with the reported numerical data [52,53,66,73] in Table 1. In addition, we provide a comparison of the maxima of velocity field, as well as the local and averaged Nusselt numbers.

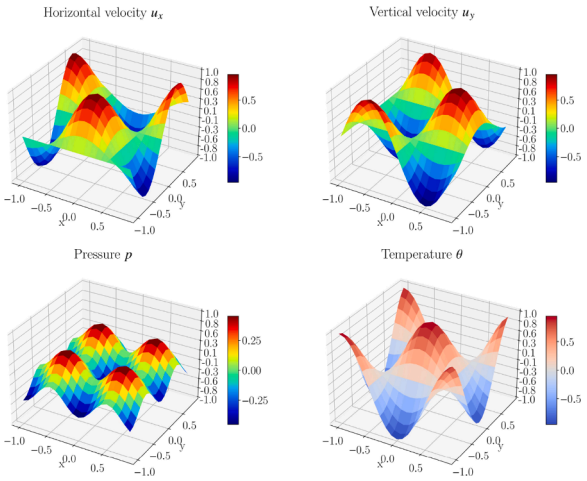


**Fig. 1.** Visualization of Beltrami flow: velocity, pressure, and temperature fields.

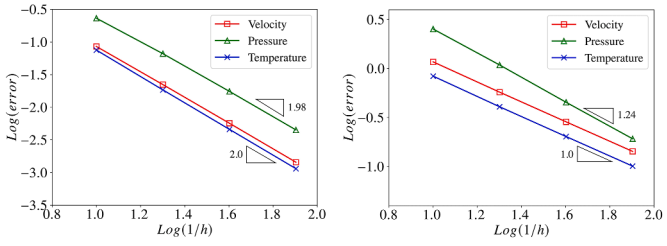


**Fig. 2.** Convergence rate plots for linear quadrilateral elements: (a) $L_2$-norm of error (b) $H^1$-seminorm of error.

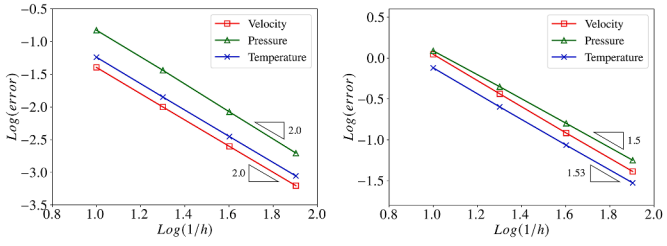


**Fig. 3.** Convergence rate plots for linear triangular elements: (a) $L_2$-norm of error (b) $H^1$-seminorm of error.

#### 5.2.1. Average Nusselt number

The average Nusselt number describes the averaged heat flux along a certain boundary and it is defined as follows:

$$\bar{Nu} = \frac{1}{A_H}\int_{\Gamma_H} \nabla\theta\cdot\mathbf{n}\ d\Gamma \tag{54}$$

As reported in the literature, Hortmann et al. [53] used a multigrid finite volume method and extrapolated the averaged Nusselt number through the finest mesh for various Rayleigh numbers with more significant digits than in the other available data. Therefore, these computed values are used as the reference data for the convergence rate study on the error of the averaged Nusselt number (i.e., the difference between the computed and the reported $\bar{Nu}$), as shown in Fig. 5.

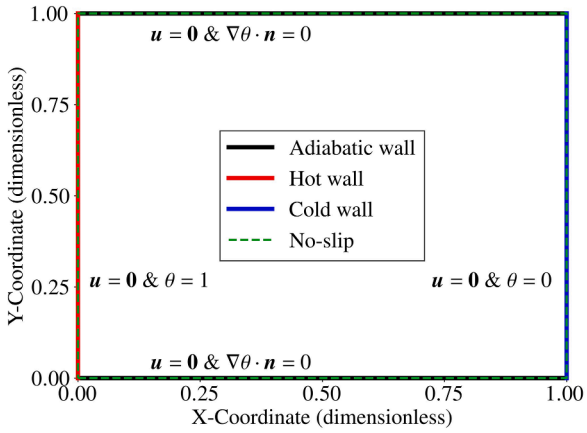


**Fig. 4.** Schematic diagram of the natural convection problem.

**Table 1**
Comparison of the average Nusselt number for different Rayleigh number flows with the data reported in the literature.

| *Ra* | $10^3$ | $10^4$ | $10^5$ | $10^6$ |
|---|---|---|---|---|
| Ref. [52] | 1.114 | 2.245 | 4.510 | 8.806 |
| Ref. [73] | 1.118 | 2.243 | 4.519 | 8.800 |
| Ref. [53] | – | 2.24475 | 4.52164 | 8.82513 |
| Ref. [66] | 1.118 | 2.245 | 4.516 | 8.810 |
| Present Work | 1.11777 | 2.24462 | 4.52021 | 8.81490 |

#### 5.2.2. *Maxima of velocities*

The maximum horizontal velocity $U_{\max}$ along the vertical middle line ($x = 0.5$) and the maximum vertical velocity $V_{\max}$ along the horizontal middle line ($y = 0.5$) is also reported in the literature [52,53,66,73]. We compare our simulations with a mesh of 200×200 Q4 elements with the reported numerical results from various numerical methods in the literature. This comparison is provided in Tables 2 and 3, where our simulation shows good agreement with the published numerical results.

### 5.3. *Tilted square enclosure with pipes*

Convective flows where thermal effects are taken into account via buoyancy force typically arise in energy related applications, namely solar collectors and heat exchangers where a pipe or a system of pipelines is arranged in a carefully designed order within an enclosure. The 2D cross sectional domain of a long rectangular tube with a cylindrical hot pipe in the middle is shown in Fig. 6. In this numerical test, we are interested in the heat exchange due to stratification between the cold walls of the square and the hot wall of the cylinder. Two design parameters for the device that are taken into account are the radius of the pipe and the orientation of the device.

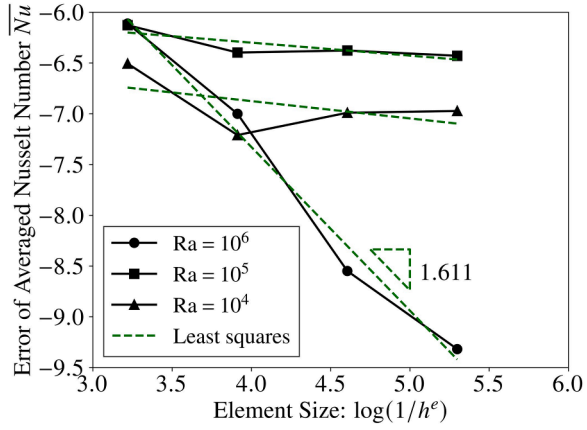


**Fig. 5.** Convergence rate of the averaged Nusselt number.

#### 5.3.1. *A single cylinder in a square enclosure with varying Rayleigh number*

The first test case considers a cylinder with radius $r = 0.2$, where the gravity force acts perpendicular to the temperature gradient. The velocity and temperature contours superposed with velocity streamlines and isothermal contours are shown in Fig. 7. The computed results are compared with the reported data in [74], where the conventional uncoupled VMS stabilization is employed. Present results are attained on a structured mesh of 5408 nodes with linear quadrilateral elements, while the reference data is computed on 6379 nodes with cubic interpolation. Figs. 8 and 9 present the distribution of the vertical velocity field and relative temperature along the horizontal and vertical centerlines, respectively. In these Figs., arclength is the accumulated length of external boundary, starting clockwise from the top-left corner.

By varying the radius of the inner circle and the angle of inclination, we run another two cases in which the radius is enlarged to $r = 0.3$ and the gravity acts at an angle of $\pi/4$ with respect to the gradient of temperature. The velocity and temperature contours superposed with velocity streamlines and isothermal contours are shown in Fig. 10.

For quantitative validation, in Fig. 11 we compare the distribution of local Nusselt number (heat flux) along the periphery of the domain and the inner circular boundaries with the reported numerical data [55] that was obtained via finite volume method on a staggered grid.

#### 5.3.2. *Four cylinders in a square enclosure*

This test case is a continuation of the previous test case on natural convection in a square enclosure where the number of inner cylinders is increased to 4. The radius of each cylinder is 0.1 and they are located asymmetrically in the enclosure with coordinates of their centers as: (0.25, 0.75), (0.75, 0.75), (0.25, 0.25) and (0.75, 0.25). Velocity contours with superposed streamlines, and relative temperature distribution with superposed isothermal contours for $Ra = 10^4$ are shown in Fig. 12. A quantitative comparison with reported data from [54] is presented in Fig. 13, where the local Nusselt number at domain boundaries and inner circles are plotted.

### 5.4. *Natural convection of nanofluid in a wavy wall enclosure*

In this section, we carry out a numerical test case on natural convection in nanofluids with the proposed method. An enclosure with wavy walls is selected to illustrate the applicability of the proposed method for complex geometries where heat transfer characteristics and entropy generation rates are less understood as compared to that in regular geometries.

The working fluid is Cu-water nanofluid and the driving mechanism of the system is a constant heat flux $\tilde{q}$ applied at the left wall. The system is quantified by Prandtl number and Rayleigh number based on the properties of the base fluid (i.e., water). In the definition of Rayleigh number in Eq. (48), the temperature gap is calculated as $\Delta T = \tilde{q}\, W/k_{bf}$, and the characteristic length scale is chosen as the width of the bottom wall $W$. Via non-dimensionalization, the kinematic viscosity in Eq. (1) is defined as $\nu = Pr\ \nu_{nf}/\nu_{bf}$, the thermal diffusivity in Eq. (3) is $\alpha = \alpha_{nf}/\alpha_{bf}$, and the thermal expansion coefficient in Eq. (1) is $\beta = Ra \cdot Pr\ \beta_{nf}/\beta_{bf}$. The material properties of base fluid and nanoparticles

**Table 2**
Maximum horizontal velocity $U_{max}$ at the vertical middle line ($x = 0.5$).

| *Ra* | $10^3$ | $10^4$ | $10^5$ | $10^6$ |
|---|---|---|---|---|
| Ref. [52] | 0.153 | 0.193 | 0.132 | 0.077 |
| Ref. [73] | 0.136 | 0.192 | 0.153 | 0.079 |
| Ref. [53] | – | 0.192 | 0.153 | 0.079 |
| Ref. [66] | 0.138 | 0.194 | 0.132 | 0.078 |
| Present Work | 0.136823 | 0.192063 | 0.130386 | 0.0769102 |

**Table 3**
Maximum vertical velocity $V_{max}$ at the horizontal middle line ($y = 0.5$).

| Ra | $10^3$ | $10^4$ | $10^5$ | $10^6$ |
|---|---|---|---|---|
| Ref. [52] | 0.155 | 0.234 | 0.258 | 0.262 |
| Ref. [73] | 0.138 | 0.234 | 0.261 | 0.262 |
| Ref. [53] | – | 0.233 | 0.261 | 0.262 |
| Ref. [66] | 0.139 | 0.235 | 0.259 | 0.263 |
| Present Work | 0.13885 | 0.232963 | 0.257658 | 0.261474 |

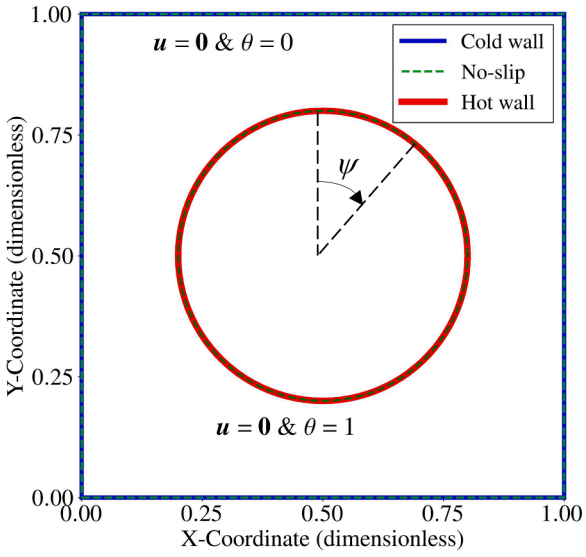


**Fig. 6.** Schematic diagram of natural convection in a 2D heat exchanger.

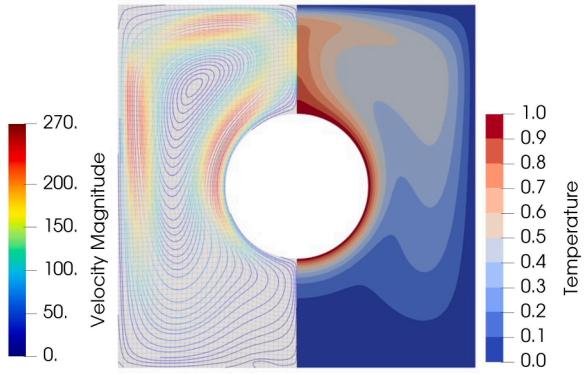


**Fig. 7.** Contours of velocity with superposed velocity streamlines (left), and relative temperature with isothermal contours (right) ($Ra = 10^4$, $r = 0.2$, 1 cylinder case).

are given in Table 4, and those of nanofluids are computed following Eqs. (8)–(12). The external forcing term $\mathbf{f}_b$ in Eq. (1) and the heat source/sink term $f$ in Eq. (3) are taken as zero. Thermomechanical properties of the base fluid and nanoparticles are given in Table 4.

The geometry consists of an enclosure of width $W$ in which left and right walls are wavy and their height is controlled by a wavelength parameter $\lambda$. The profile of the wavy wall is defined by the following equation:

$$x^* = \alpha_1 \sin\left(\frac{2\pi y^*}{\lambda^*}\right) + \alpha_2 \sin\left(\frac{4\pi y^*}{\lambda^*}\right) \tag{55}$$

where $\alpha_1$ and $\alpha_2$ are the amplitudes of two superimposed sinusoidal waves and the superscript (*) represents non-dimensionalization carried out using width $W$. For the simulations presented here we have used $\alpha_1 = 0.5$, $\alpha_2 = 0.2$, and $W = 1$.

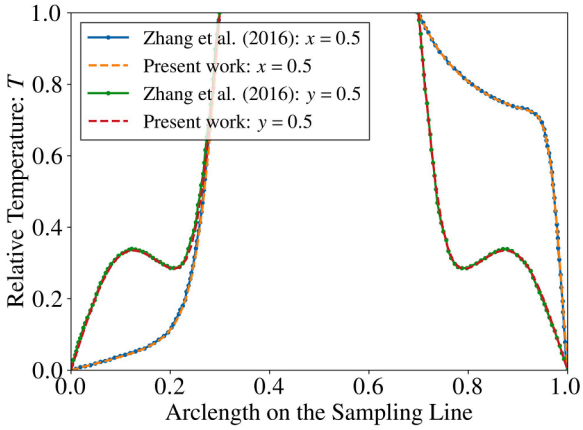


**Fig. 8.** Vertical velocity distribution along $x = 0.5$ and $y = 0.5$ ($Ra = 10^6$ and $r = 0.2$).

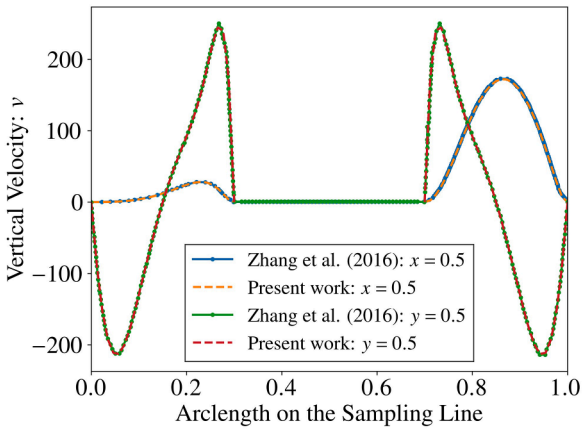


**Fig. 9.** Temperature field distribution along $x = 0.5$ and $y = 0.5$ ($Ra = 10^6$ and $r = 0.2$).

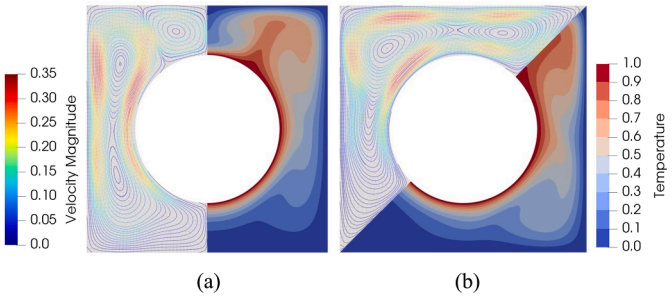


**Fig. 10.** Contours of velocity with superposed velocity streamlines (left), and relative temperature with isothermal contours (right) ($Ra = 10^6$, $r = 0.3$, 1 cylinder case): (a) Not inclined, and (b) Inclined at 45 degrees.

For boundary conditions, it is assumed that the left wall is heated by a constant heat flux $\widetilde{q}_o = k_{bf}/k_{nf}$ while the right wall is maintained at a constant low temperature ($\theta = 0$). The upper and lower walls are both assumed to be insulated (no thermal flux). Moreover, no-slip velocity boundary conditions are applied on all the wall surfaces. A schematic diagram of the problem is shown in Fig. 14. The computational grid is comprised of 100×200 linear quadrilateral elements.

The problem is run in a quasi-static fashion in which the thermal flux is applied in 10 equal load steps. We have implemented the consistent

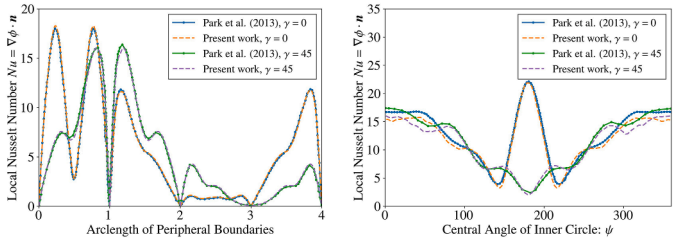


**Fig. 11.** Distribution of local Nusselt number with respect to the arclength of peripheral boundaries and central angle of inner boundary.

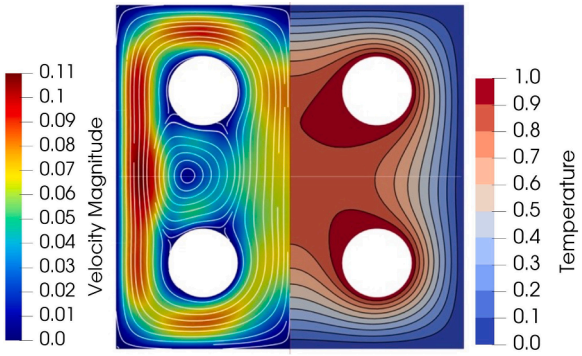


**Fig. 12.** Contours of velocity with superposed velocity streamlines (left), and relative temperature with isothermal contours (right) ($Ra = 10^4$, $r = 0.1$, 4 cylinders case).

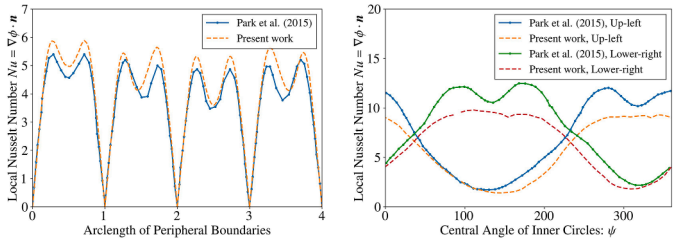


**Fig. 13.** Distribution of local Nusselt number with respect to the arclength of peripheral boundaries and central angle of inner boundary.

**Table 4**
Thermophysical properties of base fluid and nanoparticles.

| Property | Water | Cu |
|---|---|---|
| Specific heat, $C_p$ (J/kg K) | 4179 | 385 |
| Thermal conductivity, $k$ (W/m K) | 0.613 | 400 |
| Thermal diffusivity, $\alpha$ ($m^2/s$) | $1.47 \times 10^{-7}$ | $1163.1 \times 10^{-7}$ |
| Thermal expansion coefficient, $\beta$ ($m^2/s$) | $21 \times 10^{-5}$ | $1.67 \times 10^{-5}$ |
| Density, $\rho$ ($kg/m^3$) | 997.1 | 8933 |

tangent tensor and therefore quadratic rate of convergence is achieved in the nonlinear iterative solution procedure. Table 5 shows the evolution of the residual as a function of the iteration number for two representative load steps.

The transfer of heat in this problem is measured in terms of mean Nusselt number at the hot wavy wall, which is a ratio of convective to conductive heat transfer at a fluid boundary. Stronger thermal convection results in lower temperature and thus higher value of mean Nusselt number which is defined as:

$$Nu = \frac{1}{\theta_s} \tag{56}$$

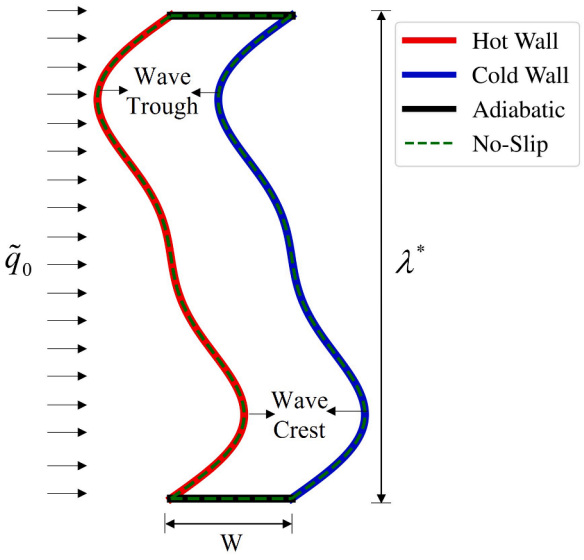


**Fig. 14.** Schematic diagram of the wavy-wall problem.

**Table 5**
Residual reduction in Newton Raphson scheme for wavy-wall problem ($\phi = 0\%$, $Ra = 10^4$, $\lambda^* = 4$).

| Iteration | Step 3 | Step 10 |
|---|---|---|
| 1 | $9.4450 \times 10^4$ | $4.8751 \times 10^4$ |
| 2 | $1.1933 \times 10^3$ | $3.5521 \times 10^1$ |
| 3 | $6.1191 \times 10^{-2}$ | $1.8736 \times 10^{-5}$ |
| 4 | $2.2284 \times 10^{-10}$ | $2.1297 \times 10^{-14}$ |

$$Nu = \frac{1}{l_w^*} \int_0^{\lambda^*} Nu \; ds \tag{57}$$

where $\theta_s$ is the temperature on the wall surface, and $l_w^*$ is the non-dimensional length of the wall. Furthermore, the local rate of entropy generation as given in [70] is as follows.

$$\dot{S}_l^* = \frac{k_{nf}}{k_{bf}} \frac{1}{(\theta + T_r)^2} \left[ \left(\frac{\partial\theta}{\partial x}\right)^2 + \left(\frac{\partial\theta}{\partial y}\right)^2 \right] + \frac{E_c Pr}{(\theta + T_r)} \frac{\mu_{nf}}{\mu_{bf}} \left\{ 2\left[ \left(\frac{\partial\theta}{\partial x}\right)^2 + \left(\frac{\partial\theta}{\partial y}\right)^2 \right] + \left(\frac{\partial u_x}{\partial x} + \frac{\partial u_y}{\partial y}\right)^2 \right\} \tag{58}$$

where $\dot{S}_l^* = W^2/k_{nf}\dot{S}_l$ is the non-dimensional rate of local entropy generation, $E_c = C_1/Ra$ is the Eckert number, and $T_r = C_2/Ra$. $C_1$ and $C_2$ are constants with values $7.940 \times 10^{-10}$ and $4.607 \times 10^6$, respectively, as given in [70]. The total non-dimensional entropy generation rate per unit volume is obtained as:

$$\dot{S}_t = \frac{1}{V^*} \int \dot{S}_l^* \; dV^* \tag{59}$$

Figs. 15 and 16 show a qualitative comparison of isotherms, velocity streamlines, and local entropy generation rate of water and Cu-water nanofluid at two Rayleigh numbers. At lower Rayleigh number, the buoyancy effect is weaker and three separate vortices are formed. However at higher Rayleigh number, these vortices expand and interact with each other due to stronger thermal buoyancy. Similarly, the isotherms at lower Rayleigh number follow the wavy surface but at higher Rayleigh number, due to stronger buoyance and vortices, these isotherms are twisted. It is also observed that the isotherms are concentrated near the wave crest region of the cold wall and the wave trough region of the hot wall giving rise to regions of local entropy generation due to increased heat transfer. At higher Rayleigh number, these regions are thinner and longer due to a thinner thermal boundary layer and

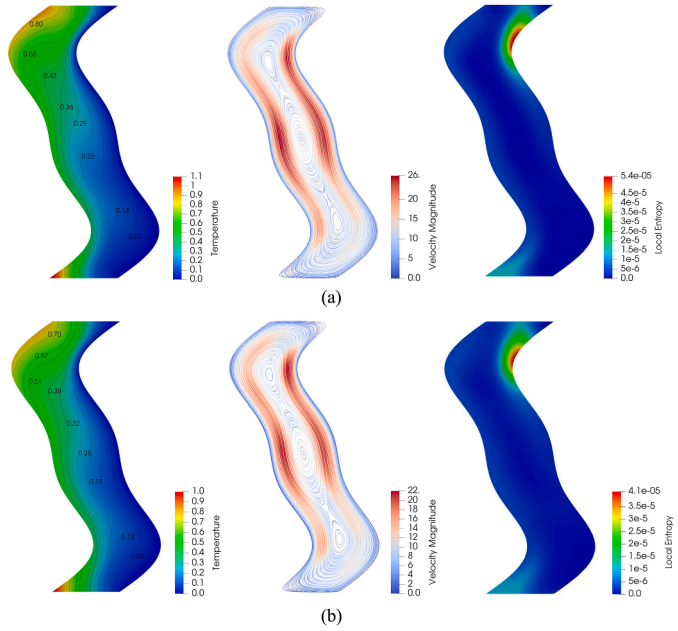


**Fig. 15.** Isotherms, velocity streamlines, and local entropy generation rate for $Ra = 10^4$ and $\lambda^* = 4$ (a) $\phi = 0\%$ (water) (b) $\phi = 10\%$.

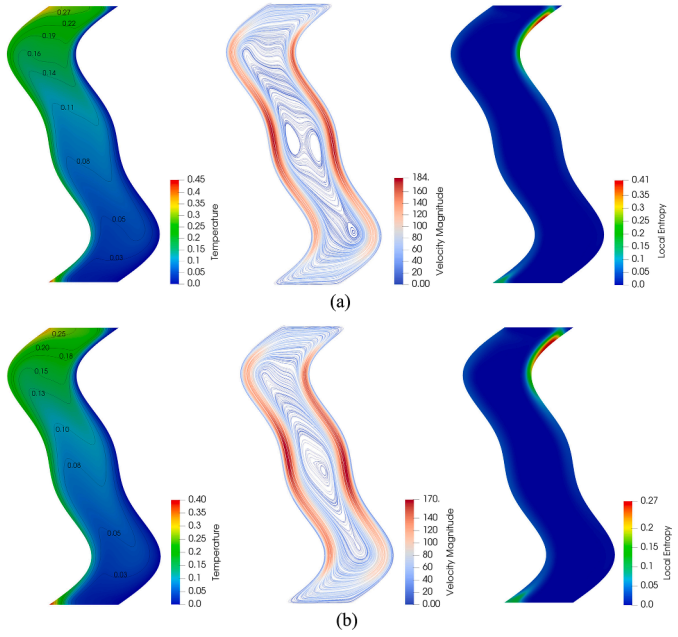


**Fig. 16.** Isotherms, velocity streamlines, and local entropy generation rate for $Ra = 10^6$ and $\lambda^* = 4$ (a) $\phi = 0\%$ (water) (b) $\phi = 10\%$.

generate higher local entropy.

Although adding nanoparticles to water for both Rayleigh numbers shows similar trend of more efficient heat transfer, the effect is more pronounced in higher Rayleigh number flow. Specifically, the maximum local entropy generation rate reduces nearly 34% in the case with $Ra = 10^6$, while it only reduces 24% in the case with $Ra = 10^4$. Along with a decreased temperature within the enclosure, these results also show the effect of nanofluids in increasing the heat transfer properties.

Fig. 17(a) shows change in the mean Nusselt number as a function of Rayleigh number for different values of nanoparticle volume fraction $\phi$. As discussed earlier, at higher Rayleigh numbers, temperature in the enclosure is lower due to the increased thermal convection that results in a higher value of the mean Nusselt number. Addition of nanoparticles also increases heat transfer, and we see a nearly linear upward trend in $Nu_m$ with an increase in the volume fraction of nanoparticles.

Fig. 17(b) shows the change in total entropy generation rate $(\dot{S}_t)$ with nanoparticle volume fraction as a function of Rayleigh number. At a given (but otherwise arbitrary) volume fraction, $\dot{S}_t$ is higher for a higher Rayleigh number due to the stronger convection effects and larger temperature gradients. However, as we add nanoparticles, both the viscosity and the thermal conductivity of the nanofluid increase as compared to that of water. Higher viscosity leads to more viscous dissipation, and in turn, increased entropy. But higher thermal conductivity results in lower entropy generation which outweighs the effect of increased viscosity and thus we see a slight reduction in total entropy generation with the addition of nanoparticles. The results in this study are consistent with that of [70].

To investigate the optimal geometric configuration of the wavy wall, a study is performed on the variation of mean Nusselt number and total entropy generation rate with the wavelength of the wavy surface as a function of the Rayleigh number. This study is significant in designing high-efficiency heat transfer systems for practical engineering applications. From Fig. 18, it is observed that although the profile varies sharply for shorter wavelengths and hence the crest and trough regions have large local Nusselt number, but the area available for heat transfer is smaller, so mean Nusselt number is lower and the total entropy generation is higher due to steeper temperature gradients in the crest and trough regions. The optimal configuration for heat transfer is found at the wavelength of 8 with maximum mean Nusselt number and lowest total entropy generation rate. Beyond the optimum wavelength, the profile varies very gently and thus there is no thermal conductivity enhancement due to geometry. We also verify the present findings by comparing them with the results given in [70].

## 6. Conclusion

This paper started with a literature review on the technical challenges encountered in the development of the class of fluids termed as nanofluids. Mathematical and numerical modeling of this class of fluids has highlighted deficiencies in the models, thereby prompting further theoretical developments. Experimental and numerical studies on the issue of statistical scatter in the properties of the particles, and consequently their effect on the rheology of the particle laden fluids has also been reported in the literature. Among the various computational techniques, finite element method has emerged as a method of choice because of its rigorous mathematical footing and due to the flexibility it provides for the modeling and analysis of flows in complex geometries.

The mathematical model for thermal fluids with nano particles consists of conservation laws for mass, momentum, and energy. A

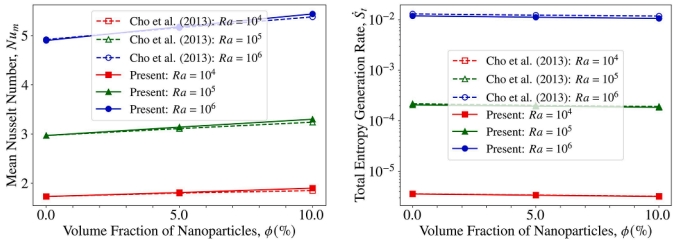


**Fig. 17.** Variation of (a) mean Nusselt number, and (b) total entropy generation rate with nanoparticle volume fraction as a function of Rayleigh number ($\lambda^* = 4$).

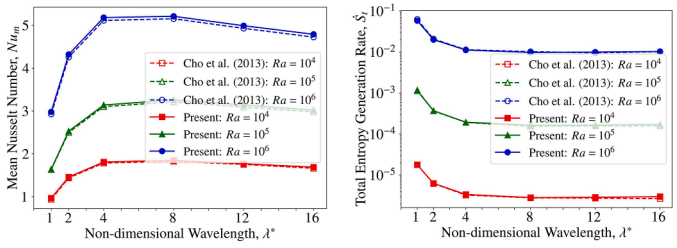


(a) (b)

**Fig. 18.** Variation of (a) mean Nusselt number, and (b) total entropy generation rate with wavy wall wavelength as a function of Rayleigh number. ($\phi = 5\%$).

Boussinesq buoyancy force is introduced in the momentum balance equation to account for the local variation in the temperature field. The energy conservation equation takes the form of convection-diffusion of temperature where the velocity field is furnished by the momentum balance equation. The thermal diffusivity that locally as well as globally depends on the volume fraction of dispersed nanoparticles in the media also accounts for the contribution of nanoparticles to the transport and exchange of heat.

We then presented a stabilized method that is derived in the context of the VMS framework and leads to consistent coupling of mechanical and thermal phases, both at the coarse as well as the fine scale levels. It is shown that the application of the bubble functions method to the derivation of fine-scale models preserves the differential operators of the governing equations in the subgrid scale formulation and leads to an explicit definition of the stabilization tensor that has cross-coupling terms for mechanical and thermal fields. This cross-coupling is shown to play a critical role in the simulation of thermal fluids where local coupling leads to anisotropy across the scales. The formulation leads to unified and concurrent solution of all the unknown fields and variational consistency of the formulation results in quadratic rate of convergence in the nonlinear iterative solution procedure.

The method is used to numerically investigate four test cases with increasing degree of complexity in the flow physics. The Beltrami flow with an analytical solution showed mathematical attributes of optimal convergence rates for linear triangles and quadrilaterals in all the solution fields. In the benchmark problem of Rayleigh-Bénard convection, we observed good agreement of averaged Nusselt number and velocity fields with the published literature for several Rayleigh numbers. These two test cases established the variational consistency and accuracy of the method. The computed physics was further validated on tilted square enclosures with several heated pipes at varying Rayleigh numbers. The results showed that the method accurately predicts thermal effects and heat transfer mechanism in heat exchangers that are employed in a variety of energy applications. Finally, we simulated natural convection of Cu-water nanofluid in a wavy enclosure. Heat transfer was found to be higher at higher Rayleigh number due to increased buoyancy. Adding nanoparticles increased both viscosity and thermal conductivity of the nanofluid. While higher viscosity led to more viscous dissipation, it in turn increased entropy. On the other hand higher thermal conductivity resulted in lower entropy generation, thereby outweighing the effects of increased viscosity and resulting in reduction in the total entropy generation and increase in heat transfer efficiency especially at higher Rayleigh number flows ($Ra = 10^6$). Numerical simulations also showed that isotherms were concentrated around the crest and trough regions of the wavy wall, giving rise to regions of local entropy generation, thereby highlighting geometric effects on the heat transfer mechanism.

## Declaration of Competing Interest

The authors declare no conflict of interest.

## Data availability

Data will be made available on request.

## Acknowledgments

This work was supported by US-NSF grant no. NSF-DMS-16-20231 to the University of Illinois. Computing resources were provided by US-NSF Teragrid/ XSEDE program under grant no. TG-DMS100004. This support is gratefully acknowledged.

## References

[1] J.C. Maxwell, Pt. II. Electrokinematics. Ch. II. conduction and resistance, in: A Treatise on Electricity and Magnetism, Vol. 1, Clarendon press, 1873, 296-297.
[2] S.U.S. Choi, J.A. Eastman, Enhancing Thermal Conductivity of Fluids with Nanoparticles, Argonne National Lab., IL (United States), 1995. No. ANL/MSD/CP-84938; CONF-951135-29.
[3] C. Garnier, J. Currie, T. Muneer, Integrated collector storage solar water heater: temperature stratification, Appl. Energy 86 (2009) 1465–1469.
[4] E.C. Okonkwo, I. Wole-Osho, I.W. Almanassra, Y.M. Abdullatif, T. Al-Ansari, An updated review of nanofluids in various heat transfer devices, J. Therm. Anal. Calorim. 145 (6) (2021) 2817–2872.
[5] J.A. Eastman, S.U.S. Choi, S. Li, W. Yu, L.J. Thompson, Anomalously increased effective thermal conductivities of ethylene glycol-based nanofluids containing copper nanoparticles, Appl. Phys. Lett. 78 (2001) 718–720.
[6] J.H. Lee, K.S. Hwang, S.P. Jang, B.H. Lee, J.H. Kim, S.U. Choi, C.J. Choi, Effective viscosities and thermal conductivities of aqueous nanofluids containing low volume concentrations of $Al_2O_3$ nanoparticles, Int. J. Heat Mass Transf. 51 (2008) 2651–2656.
[7] H. Eshgarf, M. Afrand, An experimental study on rheological behavior of non-Newtonian hybrid nano-coolant for application in cooling and heating systems, Exp. Therm. Fluid Sci. 76 (2016) 221–227.
[8] M.S. Sadeghi, N. Anadalibkhah, R. Ghasemiasl, T. Armaghani, A.S. Dogonchi, A. J. Chamkha, H. Ali, A. Asadi, On the natural convection of nanofluids in diverse shapes of enclosures: an exhaustive review, J. Therm. Anal. Calorim. 147 (2022) 1–22.
[9] A. Asadi, F. Pourfattah, I.M. Szilágyi, M. Afrand, G. Żyła, H.S. Ahn, S. Wongwises, H.M. Nguyen, A. Arabkoohsar, O. Mahian, Effect of sonication characteristics on stability, thermophysical properties, and heat transfer of nanofluids: a comprehensive review, Ultrason. Sonochem. 58 (2019), 104701.
[10] A. Asadi, S. Aberoumand, A. Moradikazerouni, F. Pourfattah, G. Żyła, P. Estellé, O. Mahian, S. Wongwises, H.M. Nguyen, A. Arabkoohsar, Recent advances in preparation methods and thermophysical properties of oil-based nanofluids: a state-of-the-art review, Powder Technol. 352 (2019) 209–226.
[11] A. Ghadimi, R. Saidur, H.S.C. Metselaar, A review of nanofluid stability properties and characterization in stationary conditions, Int. J. Heat Mass Transf. 54 (2011) 4051–4068.
[12] A.H. Pordanjani, S. Aghakhani, M. Afrand, B. Mahmoudi, O. Mahian, S. Wongwises, An updated review on application of nanofluids in heat exchangers for saving energy, Energy Convers. Manag. 198 (2019), 111886.
[13] T.W. Lin, H.C. Weng, Electrostatically stabilized nanofluids preparation by chemical co-precipitation and the effect of particle size on nanofluids viscosity, Smart Sci. 6 (3) (2018) 197–204.
[14] W. Yu, D.M. France, J.L. Routbort, S.U.S. Choi, Review and comparison of nanofluid thermal conductivity and heat transfer enhancements, Heat Transf. Eng. 29 (5) (2008) 432–460.
[15] M. Liu, C. Ding, J. Wang, Modeling of thermal conductivity of nanofluids considering aggregation and interfacial thermal resistance, RSC Adv. 6 (5) (2016) 3571–3577.
[16] R. Essajai, I. Tabtab, A. Mzerd, O. Mounkachi, N. Hassanain, M. Qjani, Molecular dynamics study of thermal properties of nanofluids composed of one-dimensional (1-D) network of interconnected gold nanoparticles, Res. Phys. 15 (2019), 102576.
[17] Y. Dehghani, A. Abdollahi, A. Karimipour, Experimental investigation toward obtaining a new correlation for viscosity of $WO_3$ and $Al_2O_3$ nanoparticles-loaded nanofluid within aqueous and non-aqueous basefluids, J. Therm. Anal. Calorim. 135 (1) (2019) 713–728.
[18] K. Khanafer, K. Vafai, A critical synthesis of thermophysical characteristics of nanofluids, Int. J. Heat Mass Transf. 54 (19-20) (2011) 4410–4428.

[19] E. MONTAZER, E. Salami, H. Yarmand, S.N. Kazi, A. Badarudin, The RSM approach to develop a new correlation for density of metal-oxide aqueous nanofluids, in: Proceedings of the IOP Conference Series: Materials Science and Engineering 210, IOP Publishing, 2017, 012071.
[20] B.C. Pak, Y.I. Cho, Hydrodynamic and heat transfer study of dispersed fluids with submicron metallic oxide particles, Exp. Heat Transf. 11 (2) (1998) 151–170.
[21] Y.R. Sekhar, K.V. Sharma, Study of viscosity and specific heat capacity characteristics of water-based $Al_2O_3$ nanofluids at low particle concentrations, J. Exp. Nanosci. 10 (2) (2015) 86–102.
[22] Y. Xuan, W. Roetzel, Conceptions for heat transfer correlation of nanofluids, Int. J. Heat Mass Transf. 43 (2000) 3701–3707.
[23] H. O'Hanley, J. Buongiorno, T. McKrell, L.W. Hu, Measurement and model validation of nanofluid specific heat capacity with differential scanning calorimetry, Adv. Mech. Eng. 4 (2012), 181079.
[24] H. Esmaeili, T. Armaghani, A. Abedini, I. Pop, Turbulent combined forced and natural convection of nanofluid in a 3D rectangular channel using two-phase model approach, J. Therm. Anal. Calorim. 135 (6) (2019) 3247–3257.
[25] D.A.G. Bruggeman, Berechnungverschiedener Physikalischer konstanten von heterogenen substanzen, I. dielektrizitatskonstanten und leitfahigkeiten der mischkorper aus isotropen substanzen, Annalen Physik. Leipzig 24 (1935) 636–679.
[26] R.L. Hamilton, O.K. Crosser, Thermal conductivity of heterogeneous two-component systems, Ind. Eng. Chem. Fundam. 1 (3) (1962) 187–191.
[27] X. Wang, X. Xu, S.U.S Choi, Thermal conductivity of nanoparticle-fluid mixture, J. Thermophys. Heat Transf. 13 (4) (1999) 474–480.
[28] P. Keblinski, S.R. Phillpot, S.U.S. Choi, J.A. Eastman, Mechanisms of heat flow in suspensions of nano-sized particles (nanofluids), Int. J. Heat Mass Transf. 45 (4) (2002) 855–863.
[29] O. Mahian, L. Kolsi, M. Amani, P. Estellé, G. Ahmadi, C. Kleinstreuer, et al., Recent advances in modeling and simulation of nanofluid flows-Part I: fundamentals and theory, Phys. Rep. 790 (2019) 1–48.
[30] O. Mahian, L. Kolsi, M. Amani, P. Estellé, G. Ahmadi, C. Kleinstreuer, et al., Recent advances in modeling and simulation of nanofluid flows-Part II: applications, Phys. Rep. 791 (2019) 1–59.
[31] W. Yu, S.U.S. Choi, The role of interfacial layers in the enhanced thermal conductivity of nanofluids: a renovated Maxwell model, J. Nanopart. Res. 5 (1) (2003) 167–171.
[32] C.S. Hirtzel, R. Rajagopalan, Invited review stability of colloidal dispersions, Chem. Eng. Commun. 33 (5-6) (1985) 301–324.
[33] S.P. Jang, S.U.S. Choi, Role of brownian motion in the enhanced thermal conductivity of nanofluids, Appl. Phys. Lett. 84 (21) (2004) 4316–4318.
[34] R. Prasher, P. Bhattacharya, P.E. Phelan, Thermal conductivity of nanoscale colloidal solutions (nanofluids), Phys. Rev. Lett. 94 (2005), 025901.
[35] Q.Z. Xue, Model for effective thermal conductivity of nanofluids, Phys. Lett. A 307 (2003) 313–317.
[36] S.K. Das, S.U.S. Choi, H.E. Patel, Heat transfer in nanofluids—a review, Heat Transf. Eng. 27 (10) (2006) 3–19.
[37] P.S. Bhattacharya, S.K. Saha, A. Yadav, et al., Brownian dynamics simulation to determine the effective thermal conductivity of nanofluids, J. Appl. Phys. 95 (11) (2004) 6492–6494.
[38] A.J. Schmidt, M. Chiesa, D.H. Torchinsky, J.A. Johnson, A. Boustani, G. H. McKinley, K.A. Nelson, G. Chen, Experimental investigation of nanofluid shear and longitudinal viscosities, Appl. Phys. Lett. 92 (24) (2008), 244107.
[39] J. Buongiorno, Convective transport in nanofluids, J. Heat Transf. 128 (2006) 240.
[40] J.C.F. Wong, Numerical simulation of two-dimensional laminar mixed-convection in a lid-driven cavity using the mixed finite element consistent splitting scheme, Int. J. Numer. Methods Heat Fluid Flow 17 (2007) 46–93.
[41] E.I. Chereches, K.V. Sharma, A.A. Minea, A numerical approach in describing ionanofluids behavior in laminar and turbulent flow, Contin. Mech. Thermodyn. 30 (2018) 657–666.
[42] M. Sheikholeslami, H.B. Rokni, Numerical modeling of nanofluid natural convection in a semi annulus in existence of Lorentz force, Comput. Methods Appl. Mech. Eng. 317 (2017) 419–430.
[43] N.A.C. Sidik, R. Mamat, Recent progress on lattice Boltzmann simulation of nanofluids: a review, Int. Commun. Heat Mass Transf. 66 (2015) 11–22.
[44] E. Abu-Nada, Dissipative particle dynamics investigation of heat transfer mechanisms in $Al_2O_3$-water nanofluid, Int. J. Therm. Sci. 123 (2018) 58. –7.
[45] F. Jabbari, A. Rajabpour, S. Saedodin, Thermal conductivity and viscosity of nanofluids: a review of recent molecular dynamics studies, Chem. Eng. Sci. 174 (2017) 67–81.
[46] Y. Li, J. Xu, D. Li, Molecular dynamics simulation of nanoscale liquid flows, Microfluid. Nanofluidics 9 (2010) 1011–1031.
[47] G. Karniadakis, A. Beskok, N. Aluru, Microflows and Nanoflows: Fundamentals and Simulation, Springer, 2006. Sci. & Busi. Media.
[48] S. Kakaç, A. Pramuanjaroenkij, Single-phase and two-phase treatments of convective heat transfer enhancement with nanofluids – a state-of-the-art review, Int. J. Therm. Sci. 100 (2016) 75–97.
[49] E.E. Tzirtzilakis, M.A. Xenos, Biomagnetic fluid flow in a driven cavity, Meccanica 48–1 (2013) 187–200.
[50] X. Jin, N.R. Aluru, Gated transport in nanofluidic devices, Microfluid. Nanofluid. 11-3 (2011) 297–306.
[51] C.R. Doering, J.D. Gibbon, Applied Analysis of the Navier-Stokes Equations, Cambridge university press, 1995.
[52] G. Barakos, E. Mitsoulis, D. Assimacopoulos, Natural convection flow in a square cavity revisited: laminar and turbulent models with wall functions, Int. J. Numer. Methods Fluids 18 (1994) 695–719.
[53] M. Hortmann, M. Perić, G. Scheuerer, Finite volume multigrid prediction of laminar natural convection: bench-mark solutions, Int. J. Numer. Methods Fluids 11 (1990) 189–207.
[54] Y.G. Park, M.Y. Ha, J. Park, Natural convection in a square enclosure with four circular cylinders positioned at different rectangular locations, Int. J. Heat Mass Transf. 81 (2015) 490–511.
[55] H.K. Park, M.Y. Ha, H.S. Yoon, Y.G. Park, C. Son, A numerical study on natural convection in an inclined square enclosure with a circular cylinder, Int. J. Heat Mass Transf. 66 (2013) 295–314.
[56] T.J.R. Hughes, G.R. Feijóo, L. Mazzei, J.B. Quincy, The variational multiscale method—a paradigm for computational mechanics, Comput. Methods Appl. Mech. Eng. 166 (1998) 3–24.
[57] M. Ayub, A. Masud, A new stabilized formulation for convective-diffusive heat transfer, Numer. Heat Transf. Part B Fundam. 44 (1) (2003) 1–23.
[58] A. Masud, R.A. Khurram, A multiscale/stabilized finite element method for the advection–diffusion equation, Comput. Methods Appl. Mech. Eng. 193 (2004) 1997–2018.
[59] A. Masud, J. Kwack, A stabilized mixed finite element method for the first-order form of advection–diffusion equation, Int. J. Numer. Methods Fluids 57 (2008) 1321–1348.
[60] R.A. Khurram, A. Masud, A multiscale/stabilized formulation of the incompressible navier–stokes equations for moving boundary flows and fluid–structure interaction, Comput. Mech. 38 (2006) 403–416.
[61] A. Masud, R. Calderer, A variational multiscale stabilized formulation for the incompressible Navier–Stokes equations, Comput. Mech. 44 (2009) 145–160.
[62] A. Masud, T.J. Truster, L.A. Bergman, A variational multiscale a posteriori error estimation method for mixed form of nearly incompressible elasticity, Comput. Methods Appl. Mech. Eng. 200 (2011) 3453–3481.
[63] K.B. Nakshatrala, A. Masud, K.D. Hjelmstad, On finite element formulations for nearly incompressible linear elasticity, Comput. Mech. 41 (2007) 547–561.
[64] L. Zhu, S.A. Goraya, A. Masud, Interface-capturing method for free-surface plunging and breaking waves, J. Eng. Mech. 145 (2019), 04019088.
[65] L. Zhu, A. Masud, Variationally derived interface stabilization for discrete multiphase flows and relation with the ghost-penalty method, Comput. Methods Appl. Mech. Eng. 373 (2021), 113404.
[66] S. Xu, B. Gao, M.C. Hsu, B. Ganapathysubramanian, A residual-based variational multiscale method with weak imposition of boundary conditions for buoyancy-driven flows, Comput. Methods Appl. Mech. Eng. 352 (2019) 345–368.
[67] J. Yan, A. Korobenko, A.E. Tejada-Martínez, R. Golshan, Y. Bazilevs, A new variational multiscale formulation for stratified incompressible turbulent flows, Comput. Fluids 158 (2017) 150–156.
[68] T.J.R. Hughes, G. Sangalli, Variational multiscale analysis: the fine-scale green's function, projection, optimization, localization, and stabilized methods, SIAM J. Numer. Anal. 45 (2007) 539–557.
[69] H.C. Brinkman, The viscosity of concentrated suspensions and solutions, J. Chem. Phys. 20 (1952) 571, 571–.
[70] C.C. Cho, C.L. Chen, C.K. Chen, Natural convection heat transfer and entropy generation in wavy-wall enclosure containing water-based nanofluid, Int. J. Heat Mass Transf. 61 (2013) 749–758.
[71] K. Khanafer, K. Vafai, M. Lightstone, Buoyancy-driven heat transfer enhancement in a two-dimensional enclosure utilizing nanofluids, Int. J. Heat Mass Transf. 46 (2003) 3639–3653.
[72] A. Masud, L.P. Franca, A hierarchical multiscale framework for problems with multiscale source terms, Comput. Methods Appl. Mech. Eng. 197 (33-40) (2008) 2692–2700.
[73] G.D. Davis, Natural convection of air in a square cavity: a bench mark numerical solution, Int. J. Numer. Methods Fluids 3 (1983) 249–264.
[74] P. Zhang, X. Zhang, J. Deng, L. Song, A numerical study of natural convection in an inclined square enclosure with an elliptic cylinder using variational multiscale element free Galerkin method, Int. J. Heat Mass Transf. 99 (2016) 721–737.